Materials Science Forum *Online: 2010-06-02*
ISSN: 1662-9752, Vol. 653, pp 87-130
doi:10.4028/www.scientific.net/MSF.653.87

Grain Growth Behavior of Al_2O_3 Nanomaterials: A Review

Ankur Gupta, Samir Sharma, Milind R. Joshi, Parnika Agrawal, Kantesh Balani[a]

Department of Materials and Metallurgical Engineering, Indian Institute of Technology Kanpur, Kanpur-208016, India

[a]kbalani@iitk.ac.in

Keywords: Nanomaterials, Al_2O_3, grain growth, grain boundary mobility, dopants/ transitions/ complexions, carbon nanotubes (CNTs).

Abstract: Emergence of engineering nanomaterials to render exceptional properties require understanding the thermodynamics and kinetics of grain growth and eliciting role of grain boundary mobility therein. Grain boundary mobility in alumina (Al_2O_3) has shown several repercussions on the evolution of microstructure to render drastic differences in the mechanical- (hardness, yield strength), optical- (transmittance), electrical- (conductivity), magnetic- (susceptibility), and electrochemical- (corrosion) properties. Consequently, the role of surface energy and the effect of temperature in equilibrating the grain shape and size are presented herewith. Several statistical or deterministic computational modeling have been attempted by researchers to elicit the dominating grain growth mechanisms. But, the limitations extend from the memory of computer and number of atoms in a simulation, or feeding the boundary conditions without incorporation of the initial microstructure to arrive at the dominating growth mechanism parameters. Contrastingly, the role of dopants in Al_2O_3 to either enhance or impede the grain growth is presented via various complexions responsible for transitions at the grain boundary interface. Six complexions resulting various grain boundary interface, strongly affect the grain boundary mobility, and sideline the dopant contributions in deciding the overall grain boundary mobility. It has also been presented that grain growth exponent increases with decreasing grain size, and additionally, secondary reinforcement of carbon nanotube (CNT) in Al_2O_3 impedes the grain mobility by as much as four times. The effect of temperature is found to be more pronounced, and has shown to enhance the grain boundary mobility by as much as six orders of magnitude.

1. Polymorphs of Aluminum Oxide

The only known oxide of aluminum occurs as Al_2O_3 (called alumina, or aluminum oxide). Alumina has more than twenty polymorphs with most stable phase being α-alumina (called corundum). Apart from α-alumina, its transition phases of alumina occur with varying temperatures and most commonly include: γ, δ, θ, η, κ, χ, β, θ', θ" and λ [1]. Though α-alumina eventually forms at high temperatures (> 1273 K), the transition to the final stage involves other transition alumina depending on the initial phase and the temperature allowed for the transition. Kinetics may encourage transition without undergoing an intermediate stage to form the stable α-alumina phase.

The crystalline alumina constitutes close packed layers of oxygen ions with aluminum ions occupying some of the available tetrahedral and octahedral sites. The polymorphism of alumina arises from the manner in which the oxygen ions are arranged in the crystal lattice positions, and the manner in which the aluminum ions occupy the tetrahedral/octahedral sites to result final ordering (or crystallinity) [2]. Al_2O_3 can be classified into either an fcc or hcp oxygen ion structure [1]. The anionic oxygen in fcc structure involves (i) γ and η in cubic form, (ii) θ as monoclinic, and (iii) δ as tetragonal or orthorhombic [1]. Whereas anionic oxygen in hcp comprises phases (i) α in rhombohedral-, (ii) κ in orthorhombic-, and (iii) χ in hexagonal- structures [1]. In addition, θ', θ", and λ phases are also observed in monoclinic structure [1].

Polymorphs of alumina can be obtained by various methods, such as thermal spraying (plasma/flame/ vapor condensation from arc), rapid quenching, vapor deposition, crystallization of

amorphous alumina, or dehydration of different alumina hydroxides [3]. All the above mentioned crystal structures of Al_2O_3 exhibit their characteristic X-ray diffraction pattern are stable at room temperature [3].

Polymorphs of Al_2O_3 are widely used in catalysis as adsorbents, support materials, binders, cutting tool wear resistant coatings, bone cement, etc [4-12]. Thermodynamic phase of α-alumina (known as sapphire) is the most stable in comparison to other transition alumina phases. Thermodynamics of α-alumina formation requires temperatures above 1000 ^{0}C (1273 K). The α-alumina is also doped with chromium to form ruby gemstone [13]. But, the solubility of α-alumina is poorer as compared to those of transition phases in electrolytic solutions, hence it limits the utilization of α-alumina in electrophoretic depositions.

Alpha-Al_2O_3 (α-alumina) is a primitive rhombohedral structure with oxygen ions in a distorted hcp lattice, and Al ions occupying two-thirds of octahedral sites. The bond lengths of Al-O are 1.86 Å and 1.97 Å [13, 14]. On the other hand γ-alumina is a tetragonally distorted spinel where Al ions occupy random tetrahedral and octahedral sites in the cubic oxygen ion structure. When the grain size is less than tens of nanometer, then high surface area (125 m^2/g) makes γ-alumina more stable than α-alumina [3]. Orthorhombic κ-alumina elicits coplanar Al-O atoms with octahedral positions preferred by Al ion near the surface [8]. The existence of δ- alumina is debated in the scientific community since Zhou and Snyder (1991) and Gan (1996) have reported absence of δ-alumina during transition from γ-alumina to θ-alumina phase. Whereas Pecharroman (1999) has detected δ-alumina by X-ray diffraction, and reported δ- alumina not as an individual phase, but a mixture of γ-alumina and θ-alumina. The θ-alumina monoclinic structure has oxygen ion in fcc lattice with Al equally occupying the tetrahedral and octahedral sites. The two Al–O bond lengths arise because of non-equal Al locations, which are 1.71–1.81 Å in the tetrahedral positions, and 1.90–2.03 Å in the octahedral positions [14]. It transforms into α-alumina at 1323 K. An intermediate phase from spinel like T to α transformation is δ* -alumina [15]. This transformation is observed sequentially that every 3/2 a in <001> direction coincide with antiphase planes of ½ [100]. Ordering results increase in the octahedral occupancy and δ* structure is described as $(Al_{0.833})[Al_{1.833}]O_4$. The ratio of octahedral to tetrahedral sites becomes 2.22 instead of 2.

β-alumina is described with the chemical formula $NaAl_{11}O_{17}$. α-alumina phase shows no long range order, but this orthorhombic structure becomes crystalline under mechanical stress or thermal treatment forming at intersplat regions of plasma sprayed/HVOF coatings [2]. Various phases of alumina are presented in the Table 1 with their density, crystal structure and temperature range of occurrence.

2. Role of Grain Boundaries in Evolving Microstructure

Almost all the properties, such as mechanical strength (yield strength, fatigue strength, etc), fracture toughness, electrical conductivity, magnetic susceptibility, corrosion behavior, etc. depends on microstructure of polycrystalline material. Additionally, the phase transitions are dictated by the interface energy available at grain boundaries towards dictating the transition. So understanding the grain growth mechanism becomes of great importance, not only for its intrinsic properties but also for its technological implications [24].

Grain growth kinetics directs the rendering of such properties with the formation of first nuclei. During solidification of the hot melt, first some atoms (20-100) form a cluster. If the size of the cluster is below the critical nuclei size at a particular temperature, material does not solidify but as the cluster of atoms achieve the critical nuclei size, Fig. 1, more and more atoms join the cluster and these clusters start growing in all the three dimensions and the solidification proceeds. At the end of solidification these clusters interrupted by the other clusters. These interrupted areas forms the grain boundary in which atoms are not arranged in a definite manner as arranged in the inner part of cluster. These

Table 1: Properties of different phases of alumina

Phase	***Density (in g/cc)***	***Bravais lattice***	***Crystal parameters (a,b,c in nm)***	***Space Group***	***Cations per unit cell***	***Temperature range* [16]**
α[1]	3.99	Rhombohedral	*a = 0.5128, α =55.33^0*	*R3c*	4	Above 1273 K
γ[1]	3.66	Cubic spinel	*a=0.79*	*Fd3m*	64/3	Below 973 K
λ [1]	---	Monoclinic	*a= 1.67, b=1.58, c= 1.185, β=115^O*	*$P2_1/c$*	64	---
K [1]	3.98	Orthorhombic	*a = 0.469, b = 0.818, c= 0.887*	*$Pna2_1$*	16	973 -1273 K
θ[1]	3.60	Monoclinic	*a = 1.185, b = 0.2904, c= 0.5622 , β = 103.8^0*	*C2/m*	8	1073-1273 K
θ'[1]	---	Monoclinic	*a = 0.967, b = 0.5586, c= 0.684 , β = 94^0*	*C2/m*	16	---
θ"[1]	---	Monoclinic	*a = 1.185, b = 1.117, c= 1.117, β = 104^0*	*A12/n1*	64	---
β [17-19]	---	Hexagonal	*a= 0.56, c= 2.253*	*$P6_3/mmc$*	---	---
X[20-23]	---	Cubic (c) Hexagonal (h) Monoclinic (m)	*(c)a = 0.795* *(h) a = 0.556 and c = 1.344 or a = 0.557 and c = 0.864* *(m) a= 1.1732, b= 0.2874, c= 0.5564*	*C2/m*	---	573-973 K
δ[1]	3.60	Orthorhombic	*a = 0.79, b = 1.58, c= 1.185*	*$P2_12_12_1$*	64	1000-1200 K
η[1]	3.66	Cubic spinel	*a=0.79*	*Fd3m*	64/3	573-973 K
δ'[1]	---	Tetragonal	*a=0.7936 ,c=2.37*	*$P4_1$*	64	---

clusters are called grains [25]. Greater the number of nuclei more will be the clusters and smaller will be the grain size. Since most of the engineering metals and ceramics are polycrystalline, their composition and crystal structure remains the same but the orientation of various planes is different, which distinguishes one grain from the other adjoining grain. Crystals are periodic arrangement of atoms in a lattice where motif repeats itself infinitely in all the three directions [26, 27]. Single crystals show anisotropic properties making it direction dependent, whereas polycrystalline materials may or may not show isotropic properties due to random orientations of fine crystals that constitute the material [28]. If the angle between two grains is more than 10 degree, these grain boundaries are called high angle grain boundaries [29]. High angle grain boundaries have high surface energy and these grain boundaries serve as preferential sites for solid state reactions such as phase transformations, diffusion and precipitation reactions.

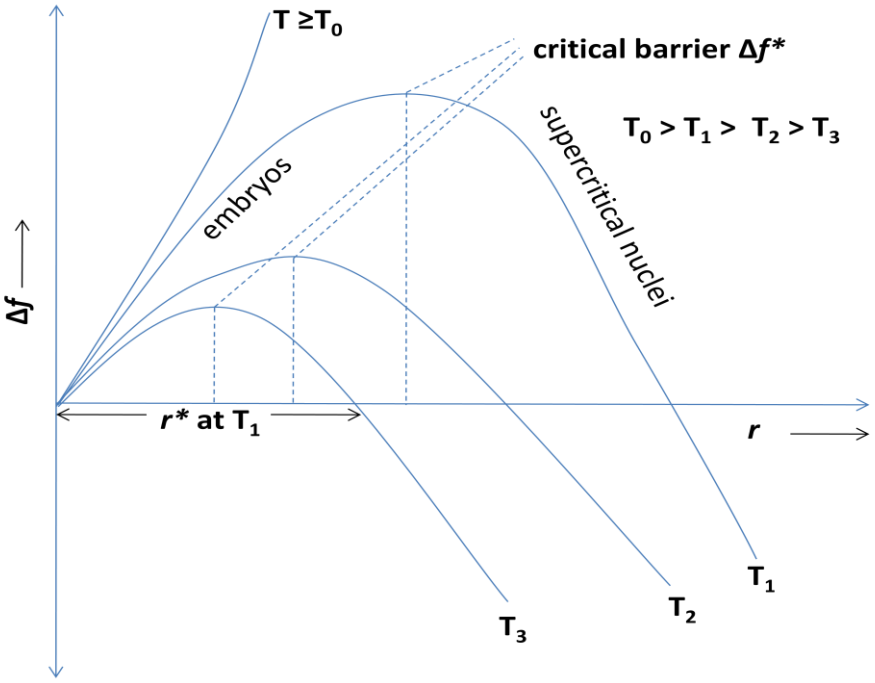

Figure 1: Effect of temperature on the critical nuclei size. Adapted from [25].

Nanomaterials have become the heart of new advanced research. Nanomaterials as the name indicates the size of the particles and the grains in the compacted materials are of the order of nanometer. So we can broadly classify them on the basis of their dimension. One dimension materials involve thickness of nanometers in one-dimension only, and other two dimensions are bigger, which implies that one-dimensional nanomaterials are like thin films. Materials those have nano scale in two dimensions include nano wires and carbon tubes, and the last class of nanomaterial with all the three dimensions in nano scale includes precipitates, colloids, etc [30]. Nano crystalline materials whose grain size also falls in the same category is generally represented as ***nc***.

Increased surface area and quantum effect are two basic things which causes changes in property of nanomaterials from conventional microstructural materials [30]. As the particle size decreases, number of atoms present on the surface increases. This effect has been presented in table 2 and Fig. 2. Shell size is defined by the number of layers of atoms with respect to the central atom. Only the surrounding atoms on the surface take part in the interaction with the environment. Hence, as the size decreases (or number of shells decrease), atoms per cluster on the surface increase and thus enhance participation of these atoms with the environment.

Table 2: Number of surface atoms in FCC nanoparticles.

Shell Number	*Diameter of Al Atoms*	*Number of Atoms in FCC Nanoparticles*		
		Total	*On Surface*	*% Surface*
1	1d	1	1	100
2	3d	13	12	92.3
3	5d	55	42	76.4
4	7d	147	92	62.6
5	9d	309	162	52.4
6	11d	561	252	44.9
7	13d	923	362	39.2
8	15d	1415	492	34.8
9	17d	2057	642	31.2
10	19d	2869	812	28.3
11	21d	3871	1002	25.9
12	23d	5083	1212	23.8
25	49d	4.90×10^4	5.76×10^3	11.7
50	99d	4.04×10^5	2.4×10^4	5.9
75	149d	1.38×10^6	5.48×10^4	4
100	199d	3.28×10^6	9.8×10^4	3

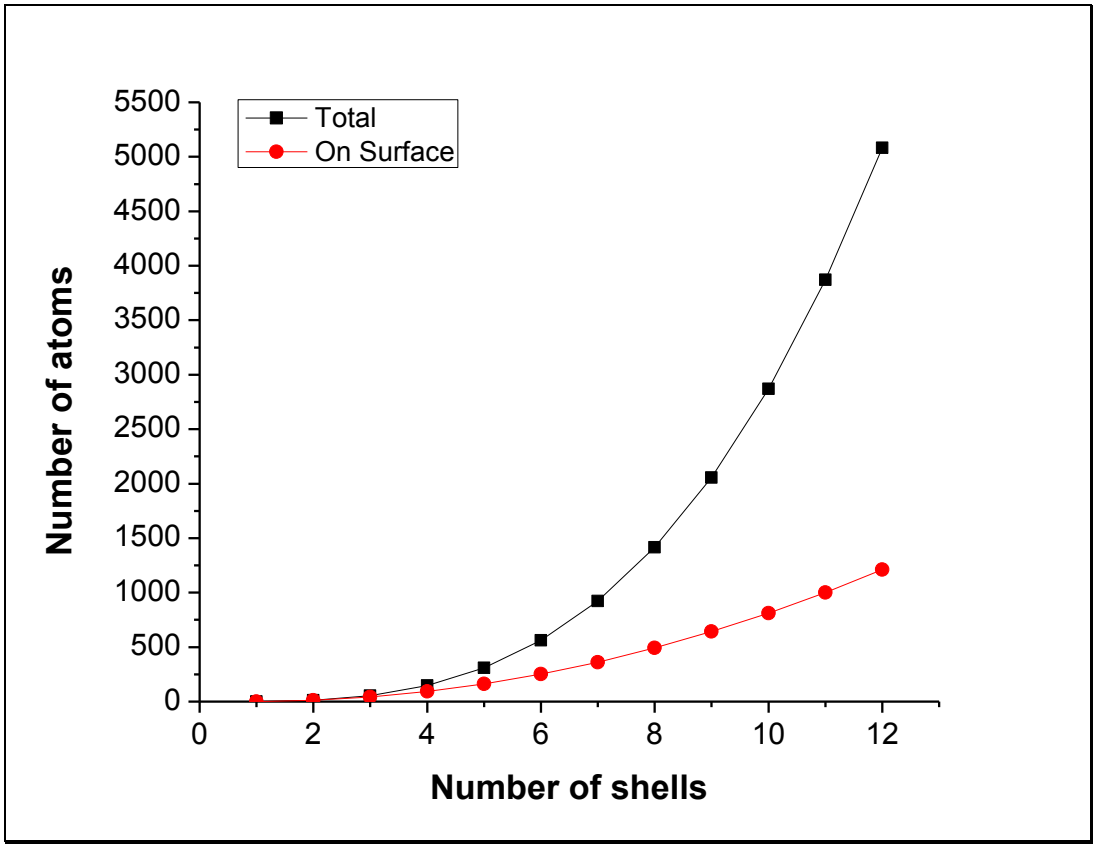

Figure 2: Comparison of total and on surface atoms as a function of number of shells.

Catalytic chemical reactions always occur at the surface and due to high surface area; nanomaterials increase the reaction rate if they are being used as a catalysts. Grain growth is also a surface phenomenon; similar to a catalytic chemical reaction; if it is getting affected only by surface area. So nanomaterials are much more reactive compared to their large particle counterparts, and the material size should be as small as possible if the rate of reaction is to be enhanced. Concurrently, quantum effect also dominates, Fig. 3, towards deciding the properties (mechanical, electrical, optical, magnetic, etc) of materials as the size reduces to few atomic clusters. Fig. 3 shows, in the quantum dot, density of electrons is constant corresponding to each energy level but as we move from 0D (quantum dot) to 3D (bulk) density of electron is not remain constant to energy level. In the case of 2D, electron density is a stepped function and in 3D, it forms a continuous function and density of electron increases with increase in energy. Now, the number of interfaces also increase as the particle size decreases and these interfaces become the dominating factors in contribute to the mechanical-, electrical-, and other properties.

Nanocrystalline materials tend to exhibit increased strength, hardness, improved toughness, reduced elastic modulus and ductility, enhanced diffusivity, higher specific heat, enhanced thermal expansion coefficient (CTE), and superior soft magnetic properties in comparison with conventional polycrystalline materials [31]. Additionally, fine grain size arrests the defects propagation and gives strength when the material is stressed.

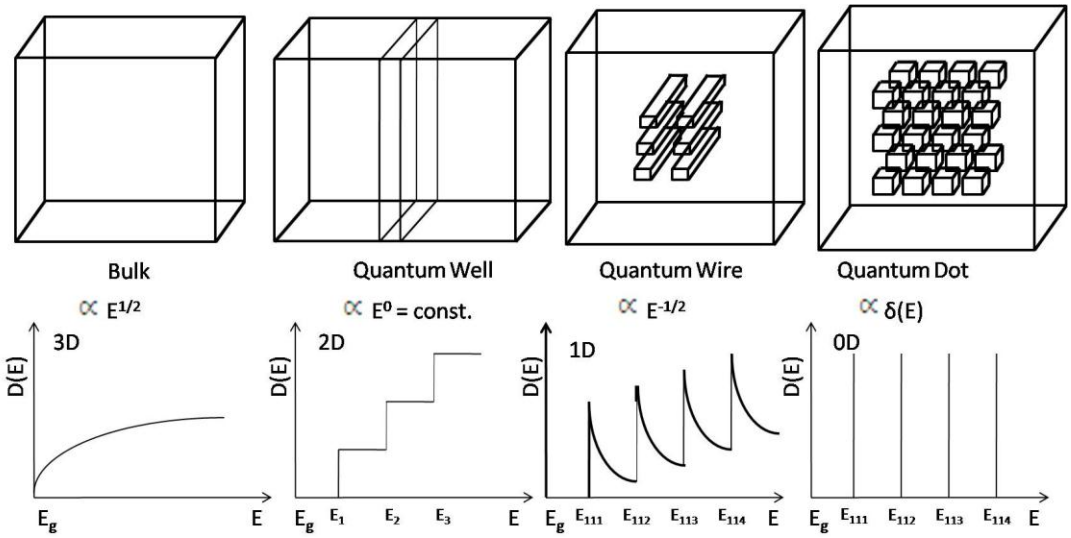

Figure 3: Change in energy density with dimensions.
Adapted from www-opto.e-technik.uni-ulm.de/lehre/cs/.

There are mainly two approaches of synthesis of nanomaterials, bottom up and top down. In the bottom up approach, high density plates arise due to lamellar structure and associated stacking faults. During integration of material from atomic to bulk structure, incomplete bonding and incomplete sintering leads to void formation. Hence, the former one (bottom up approach) results porosity and incomplete bonding between the grains. These processing flaws are detrimental for the nanocrystalline materials. Sanders et al reported in their work that as the porosity increases, Young`s modulus decreases in case of Cu and Pd [32]. Wachtman and MacKenzie derived an equation using mechanics simulation for the reduced value of modulus (E) [33, 34].

$$E = E_o (1 - f_1 p + f_2 p^2) \quad (1)$$

where E_o is the Young's modulus in fully dense condition, p is the porosity and f_1 and f_2 are equal to 1.9 and 0.9, respectively. Since yield stress and tensile ductility are related to Young`s modulus, they also get affected simultaneously. Decrease in the elastic modulus can also arise because of

different crystal structure (i.e. crystal structure mismatch at hcp/fcc interface) [35], leading to incoherent or semi-coherent registry of atoms in Co matrix, as shown in Fig. 4.

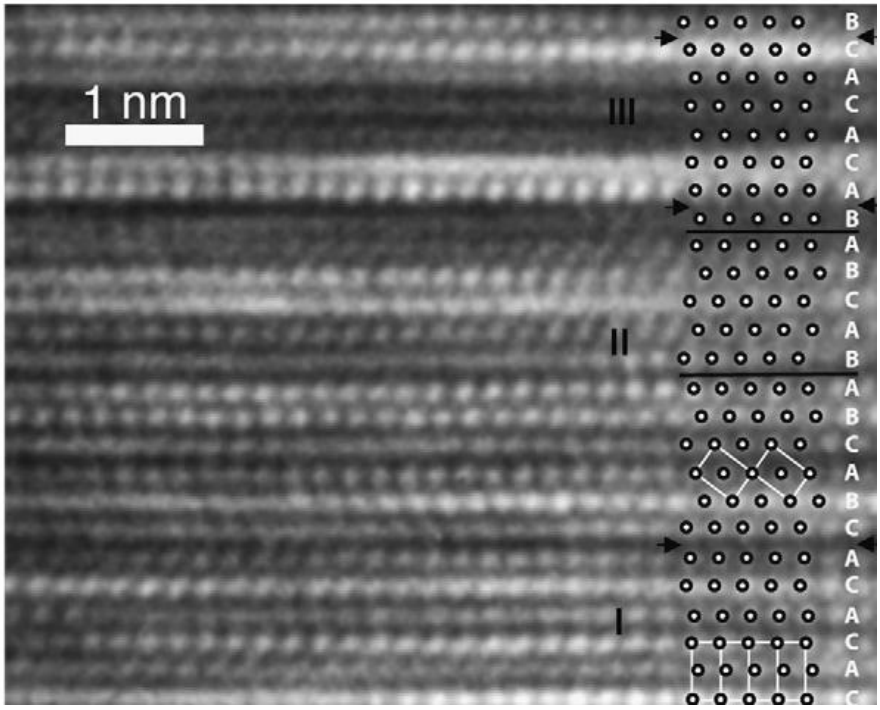

Figure 4: A high resolution TEM image of Co alloy showing high stacking fault regimes marked with arrows. Reprinted with permission from [35].

Effect of porosity on Young`s modulus is presented in Fig. 5 [32]. These existing pores provide initiation sites for the failure. Fig. 6 shows that as the grain size of Cu decreases, yield strength increases and ductility also decreases [32]. Failure is occurring at much lower strain values (<0.01) with respect to conventional grain of 20 micrometers (>0.03). Sanders et al also reported the effect of various methods of measuring the tensile behaviour.

Hall-Petch Relation gives the relationship between yield stress and grain size.

$$\sigma_o = \sigma_i + kd^{-0.5} \qquad (2)$$

where, σ_o is the yield stress, σ_i the friction stress, representing the overall resistance of the crystal lattice to dislocation movement, k is the locking parameter, and d is the average grain diameter.

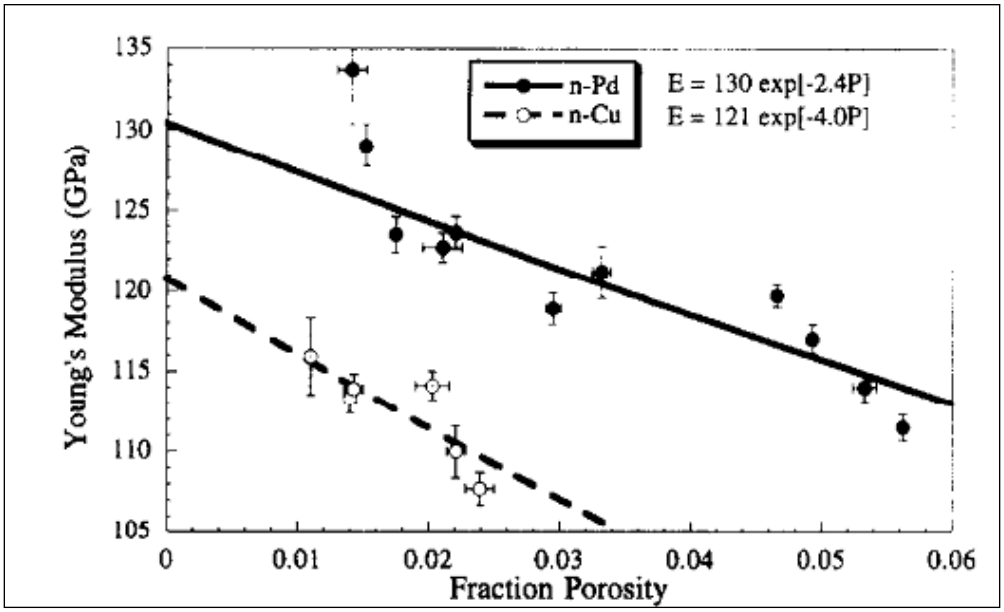

Figure 5: Effect of porosity on Young`s modulus. Reprinted with permission from [32].

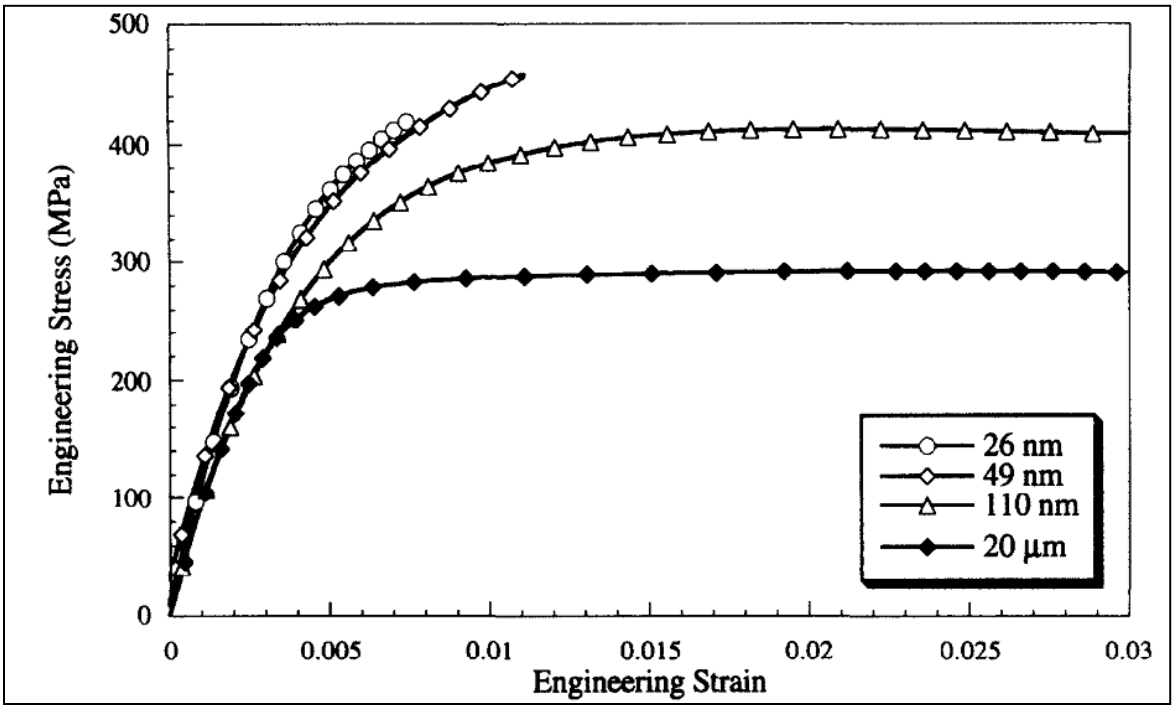

Figure 6: Effect of grain size of engineering stress-strain curve. Reprinted with permission from [32].

According to the Hall-Petch relationship, yield stress increases as the average grain size reduces. But this relation is valid only up to a certain grain size, below which the material becomes soft. This grain size is called critical grain size. As the size reduces below the critical grain size, negative Hall-Petch effect observed. This negative Hall-Petch phenomenon was first reported by Chokshi et al. on nanocrystalline Cu and Pd synthesized by inert gas consolidation [36]. In addition, Chattopadhyay also has done significant work on the negative Hall-Petch, stating that Coble creep becomes the main deformation mechanism because of rapid rate of diffusion at room temperature [37]. Fedorov and Yu have proposed a model based on the diffusional creep at room temperature, but realized that below a critical grain size, Hall-Petch relation is no more valid [38]. According to Mayer et al. the value of critical grain size is 25nm [31]. Fig. 7 is showing the hardness variation with grain size. This consists of two regimes. Regime I show a formation of plateau and Regime II

shows a decrease [39]. Here, as grain size decreases, hardness increases till it attains a peak (corresponding to critical grain size, generally 25nm), and then the hardness decreases.

Cao also observed the lower value of hardness for nanocrystalline Fe-0.5%C and Fe-4.5%C measured via Hall-Petch relationship [40]. He also reported that the value of bulk and Young`s modulus decreased with free carbon content. Fig. 8 represents various systems which show negative Hall-Petch effect [31, 39]. Negative Hall Petch effect is also reasoned to the unlikeliness of the intragranular dislocations to be active. In addition, nanotwins increase and other mechanical properties (such as yield strength) since thin twin boundaries act as coherent boundaries to induce lattice strains and resist dislocation movement.

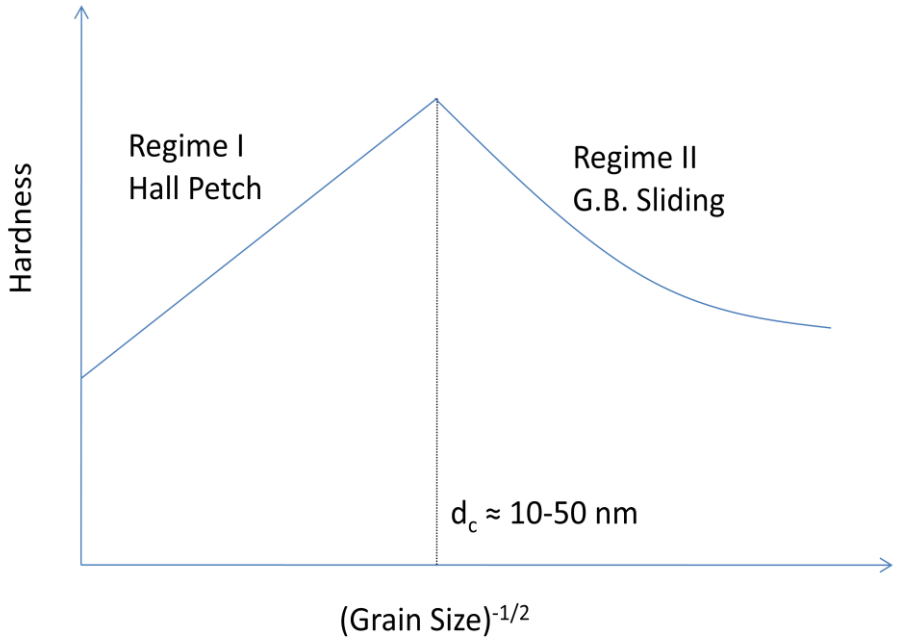

Figure 7: Generic variation of hardness with grain size and Hall-Petch regimes. Adapted from [39].

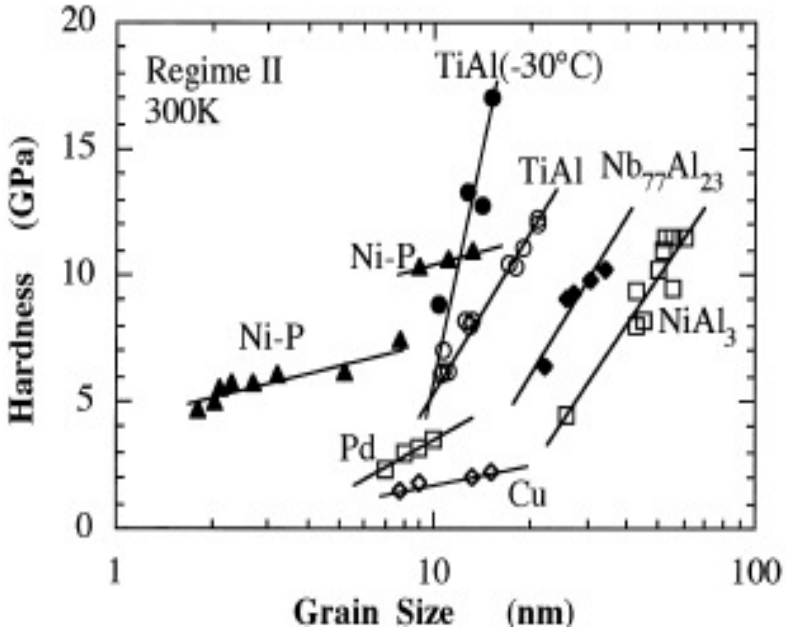

Figure 8: Various systems eliciting negative Hall-Petch effect. Reprinted with permission from [39]

Ductile metals show considerable elongation during tensile test and eventually fail by necking due to rapid increase in local stresses. Generally, in conventional size regime (tens to hundreds of micrometer) ductility increases with decrease in the average grain size. So, ideally nanomaterials should elicit enhanced ductility, but conversely it is found that ductility is usually much lower in the nanomaterials [32]. Shen et al produced nano-twins in ultrafine-grained Cu, and reported that nanotwins worked as obstacles for dislocations and increased the tensile strength and ductility [41].

Fig. 9 shows a schematic of twin structure in the nanocrystalline material, wherein nano twin Cu fractures much earlier (less ductility ~13%) as compared to that of conventional Cu. But the tensile strength can be as high as 3-4 times higher than that of conventional Cu. If twin lamellae are thick, dislocations pile up and stress concentration develops at twin boundaries but if twin lamellae are too thin only one dislocation will pass at a time and very high stress will be required to cross the twin boundary [41, 42]. Tensile instability crack nucleation or shear instability and artifacts from processing are the reasons behind the limited ductility in nanomaterials [43].

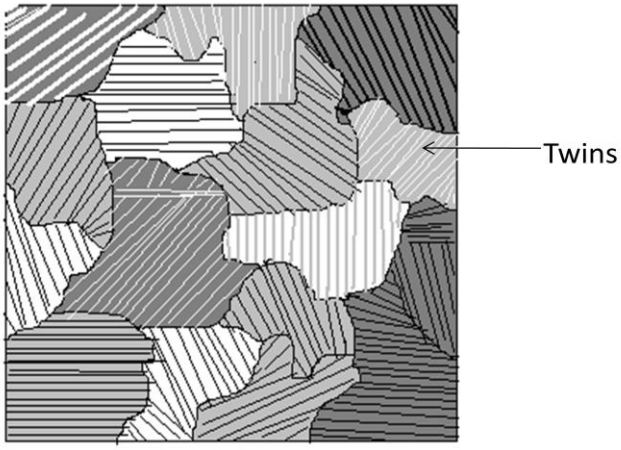

Figure 9: Schematic of nano-twins in Cu sample. Adapted from [41].

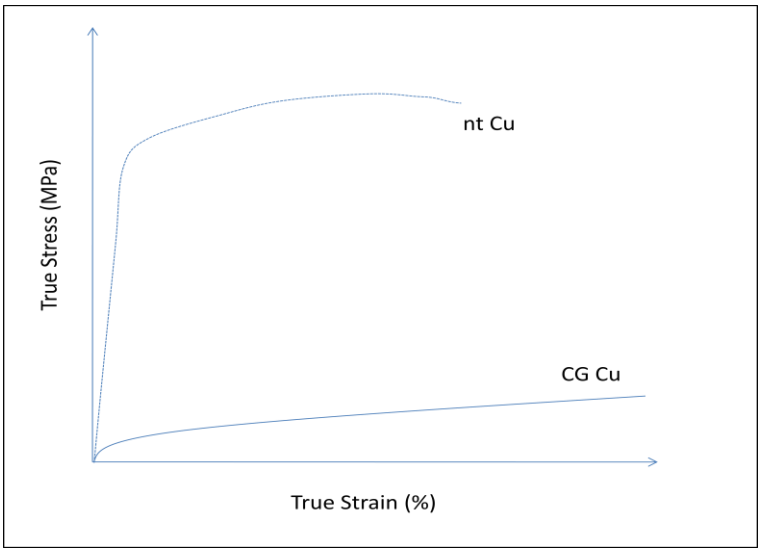

Figure 10: Comparison of ductility and flow stress between nanotwin (nt) and conventional grain (CG) size Cu. Adapted from [41].

Zheng and Zhang performed molecular dynamic simulation to understand the effect of voids on the deformation behavior [44]. They observed that initial ellipsoidal void gets blunt during

deformation process and voids do not propagate along the grain boundary, instead, shear plane forms due to voids because of:

(1) leading void tip causes emission and propagation of dislocations leading to intergranular slip
(2) void located at a triple junction facilitates the alignment of grain boundaries via grain rotation
(3) voids extend shear plane splitting of grains into two via forming grain boundary

Recently, optically transparent ceramics have become sought materials because of their requirement in many applications like self guided ballistic missiles, transparent armors, ballistic windows, optical lenses, LEDs etc. To make the materials optically transparent, grain size after processing should be made as small as possible to allow the light to pass through without scattering. Nanomaterials are found very suitable for them but the nano size powder should not have tendency to agglomerate which is the main drawback associated with nanopowders. Agglomeration causes problems in eliminating the last hundreds of pores which reduces the transmittance and thus decreases the visibility [45]. Fig. 11 shows the effect of porosity and crystallinity, i.e. for optically transparent materials. Single crystals are best because of absence of porosity [28]. But processing of single crystal is uneconomical and very complicated. Thus polycrystalline materials with almost zero porosity are preferred for serving as transparent wear-resistant ceramics.

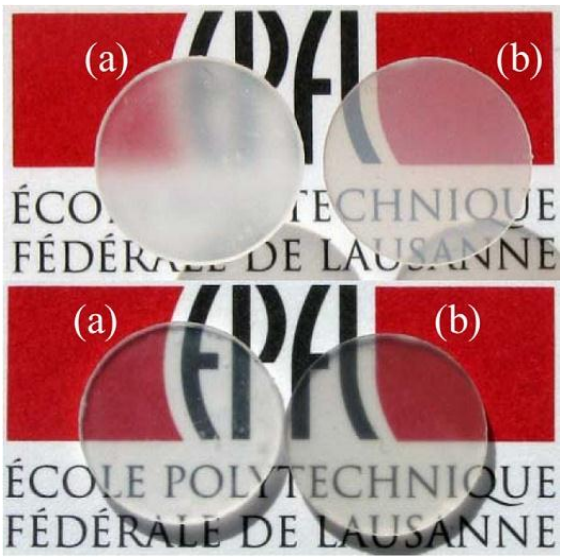

Figure 11: Effect of porosity in polycrystalline alumina on optical property. Reprinted with permission from [46].

Fig. 12 shows various types of losses in the incident beam which reduces the visibility. The pores present in the material scatter the ray of light by diffusion scattering. According to this schematic, some reflection occurs when incident beam enters the material and the same happens at the time the beam leaves another surface of the material [47]. Grain boundaries also scatter the light due to change in the refractive index between the grain and grain boundary. Thickness of the material also affects the transmittance of the light beam. This loss of transmittance is called birefringent scattering losses, which generally occurs in the polycrystalline materials [47]. Effect of thickness on transmittance also has been presented in Fig. 13.

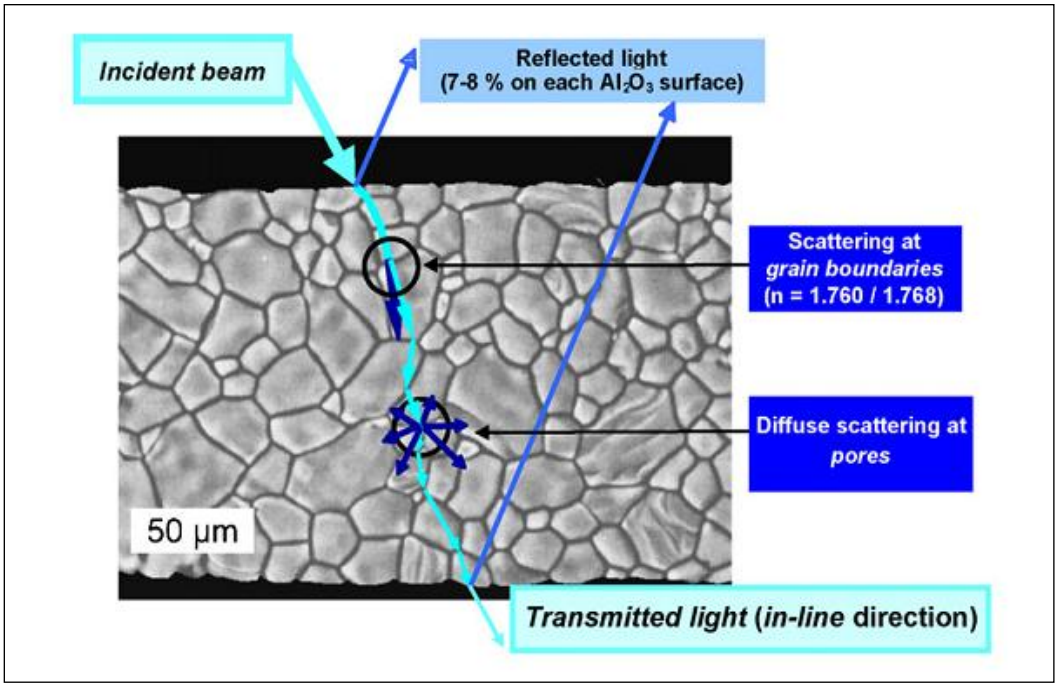

Figure 12: Various types of losses in transmittance. Reprinted with permission from [47].

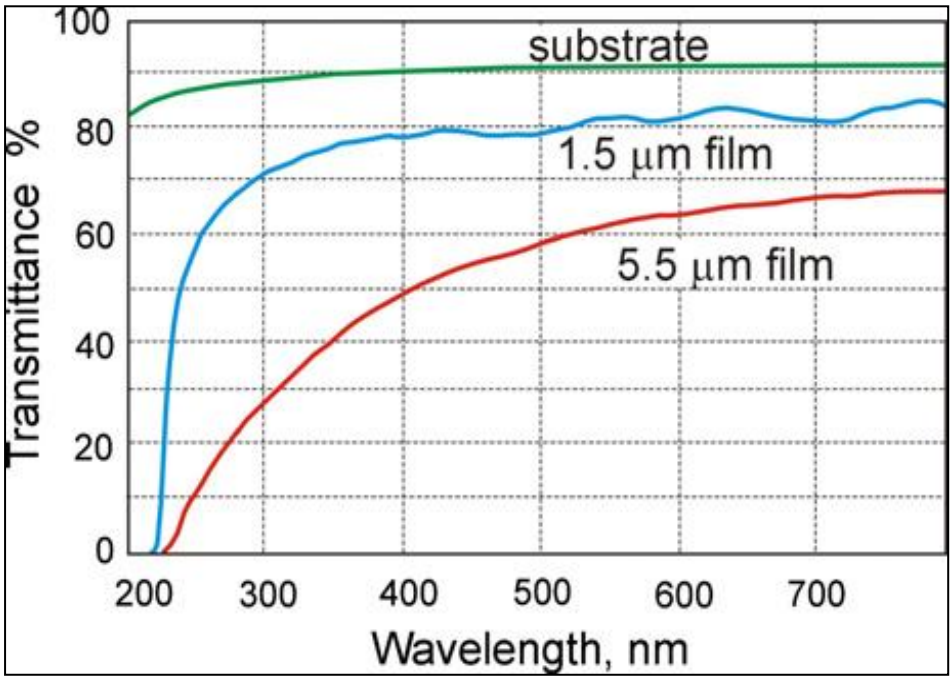

Figure 13: Effect of thickness on transmittance. Reprinted with permission from [48].

Material processing characteristics also affect the optical property. There is very narrow window of processing parameters to obtain the optical transparency. There are various techniques available to produce optically transparent alumina. Various alumina deposition techniques are summarized in Table 3.

Table 3: List of deposition techniques to produce transparent alumina film and their nature

S. No.	*Name of Technique*	*Deposited Film Nature*
1	Magnetron sputtering [49, 50]	Crystalline
2	Sol-gel [51, 52]	Crystalline
3	Pulsed laser deposition [53]	Crystalline
4	Chemical vapour deposition [54]	Crystalline
5	Aerosol-jet deposition [55, 56]	Crystalline
6	Electron beam deposition [57]	Amorphous
7	Electrophoretic deposition [58]	Amorphous

Jiang et al. [45] produced transparent polycrystalline Al_2O_3 by using spark plasma sintering. The main aim of his work was to produce optically transparent polycrystalline alumina for IR window used in missile. This application requires properties of high hardness at high temperature and transparency to IR band for short wavelengths (3-5 μm) or long wavelengths (8-12 tm). Sapphire and spinel is ideal candidate for the application but the intricate shapes processing cost is very high due to this polycrystalline alumina could be good substitute of them because its transmittance is comparable with sapphire in mid IR band as well as visible region [59]. Conditions in spark plasma sintering (SPS) are similar to conventional one but advantage associated with SPS processing is high heating rate and simultaneous application of pressure results low grain growth and high densification. As mentioned above, processing parameters also affect the transmittance, and Fig. 14 represents the effect of grain size on transmittance [45].

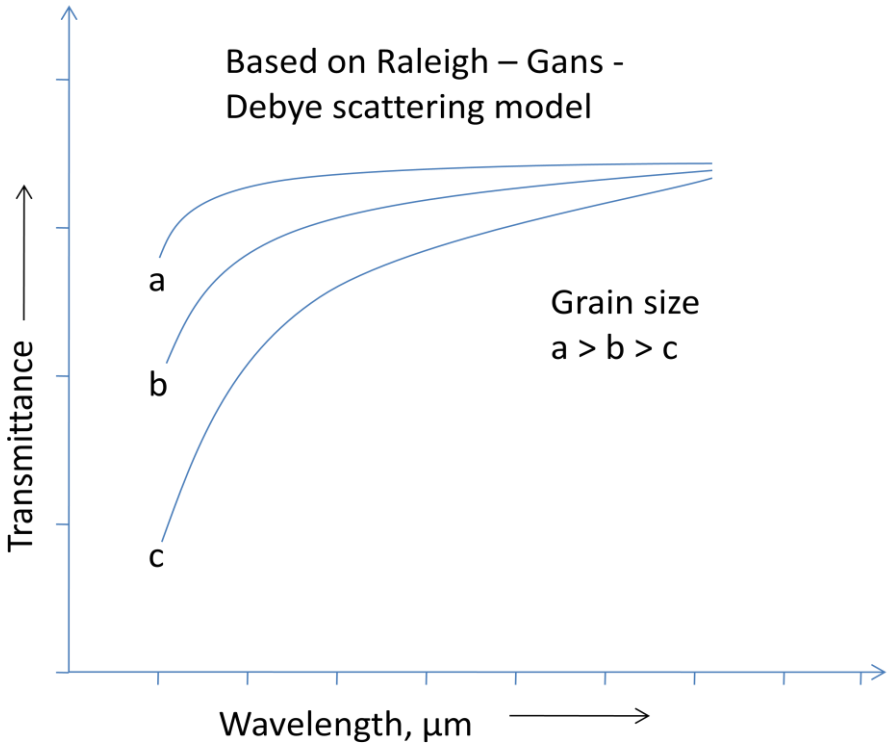

Figure 14: Effect of grain size on transmittance. Adapted from [45].

Lebedev and Krumdieck used the aerosol-jet deposition technique to produce alpha alumina on glass substrate [48]. High jet velocity to form aerosol led to fragmentation of particles, and grain sizes less than the initial powder resulted. Aerosol-jet deposition technique was performed at room temperature, wherein transmittance of 83% and 68% (in the visible region of 800 nm) was reported in 1.5µm and 5.5 µm thick alumina films respectively. This appears to be a promising future technique for the fabrication of transparent film on the glass and polymer substrates.

3. Thermodynamics and Kinetics of Grain Boundary Mobility

Grain boundaries are regions where orientation of two or more grains is adjusted to maintain continuity of bulk material. Herein, internal energy is stored in material via high atomic disorder matching along the grain boundaries. Thereby reduction of the overall energy is driven by the decrease in the grain boundary area [60, 61]. Decrease in the grain boundary area, thus, implies (i) increase in the grain size, and (ii) decrease in the internal stored energy, which is the driving force for grain growth. As the grain size increases, grain boundary interfacial free energy decreases, thereby increasing the thermodynamic stability.

It has been pointed out by Carpenter and Elam that grain growth (in tin-antimony alloy) occurs by grain boundary migration, and not by coalescence of neighboring grains [62]. It was also observed that the rate of grain boundary migration does not remain constant, and even the migration direction may change while the grain coarsening is predominant. Additionally, it might also happen that a grain growing into its neighbor is being consumed by another grain from another side. A key finding in their work also constituted that the disappearance of grains is more rapid at end in comparison to that their consumption of grain during grain growth. It has also been reported by Sutoki that a curved grain boundary tends to migrate toward its centre of curvature [63]. Harker and Parker used a statistical technique and confirmed that when grain boundaries in a single phase meet at angles other than 120 degrees, then the grains at obtuse angle (> 120 degrees) consume the grains meeting at acute angles (<120 degrees) [64]. So, essentially all angles tend to become 120 degrees upon reaching equilibrium.

The driving force for grain growth is dictated by: (i) decrease in the residual strain energy, i.e. recrystallized grains become more perfect at the expense of less perfect grains upon heating [65], and (ii) decrease in the interfacial energy, i.e. decrease in the grain-boundary area leads to the coarsening of grains [66]. Though the assumption that the driving force is a difference in the residual strain energy of the grains may explain recrystallization related to the grain growth, but this assumption fails to comment cannot explain impediment of grain growth stops upon melting of grain boundary. Consequently, if the grain growth was driven by difference in residual strain energy of adjacent grains, even a liquid layer would cause grain coarsening by redeposition of more-strained grain to less strained grain through liquid interlayer [67].

Burke and Turnbull [67] derived a parabolic relationship for the grain growth conceptualizing that grain boundary movement occurs under the effect of surface tension. Thus, atom transportation across the grain induces grain boundary migration toward the grain boundary's center of curvature to reduce the grain boundary area, minimizing the free energy. The pressure difference across the grain boundary (p) is related to the grain boundary velocity (v) as:

$$v = Mp \tag{3}$$

where, M is the grain boundary mobility. Where p can be evaluated from the radii of curvatures of the grains (r_1 and r_2) as:

$$p = \gamma\left(\frac{1}{r_1} + \frac{1}{r_2}\right) \tag{4}$$

Where, γ is the surface tension.

To evolve a relation between the grain size and grain growth rate, Burke and Turnbull made generalized assumptions of γ being independent of grain size and grain growth remaining constant for all grains, and that the radii of curvature of the grains being directly proportional to the average diameter of total grains i.e. $r \propto D$ [67]. It was also assumed that the grain growth rate (dD/dt) is directly proportional to $G = K\gamma V/r$, (where V= gram atomic volume, K'= rate constant). Now, the grain growth rate can be written as [67]:

$$\frac{dD}{dt} = \frac{K\gamma V}{D} \tag{5}$$

Which upon integration (from Do to D) provides,

$$D^2 - D_O^2 = K\gamma Vt \tag{6}$$

Where, D_O is the initial grain size (at t=0), and γ (surface tension) and V (gram atomic volume) are constant, so we can write the above equation as:

$$D^2 - D_O^2 = Kt \tag{7}$$

It is well assumed that $D_O << D$, which further gets simplified to:

$$D^2 = Kt \tag{8}$$

$$D = Kt^{1/} \tag{9}$$

and

$$D = Kt^{1/n} \tag{10}$$

Where, n is the grain growth exponent, whose maximum value is 2. From equation (10) we can directly relate the grain diameter with time.

Grain-boundary annihilation can also be used to describe the mechanism of grain growth. Herein, the grain size increase with time is due to the annihilation of grain boundary, which occurs via disappearance or rearrangement of grain boundaries [68]. Smith predicted that neighbor switching and three sided grain annihilation were two possible mechanisms to cause 2D grain growth [68]. To understand the grain annihilation the simplest model is 2D model i.e. grain growth in polycrystalline thin film, foil, and absorbed layer. The 2D polycrystal model assumed that all the

grain boundaries met at triple junctions, and the topological changes during transformation can be described by Euler's equations [69]:

$$3\Delta V = 2\Delta E = 6\Delta F \quad (11)$$

Where,ΔV, ΔE, and ΔF are the change in the number of vertices, number of edges and number of faces or grains respectively as a result of the transformation. If we consider the neighbor switching, Fig. 15(a), there is no grain disappearance and only the edges and vertices are rearranged. And the change in the number of edges, vertices and faces becomes zero. During the three-sided grain annihilation, Fig. 15(b), ΔV =2, ΔE = 3, and ΔF =1. And it follows the Euler's equation (eq. 11). For four-sided grain annihilation, Fig. 15(c), ΔV = 2, ΔE = 3, and ΔF =1 is also seen to obey the above rule (eq. 11). Similarly, in the case of five-sided grain annihilation, Fig. 15(d), two grains lose a side, two grains remain unchanged, and one grain gains a side. In this process ΔV = 2, ΔE = 3, and ΔF =1 complying with Euler's equation.

Grain annihilation was defined by Von Neumann and Mullin via rate of change of the area of an individual grain directly proportional to number of sides (n) of that grain, as [70, 71]:

$$\frac{da}{dt} = \frac{1}{3} m\gamma\pi(n-6) \quad (12)$$

Where, *da/dt* is the rate of change of an individual grain with grain area a, in time t, *n* is the number of sides of the grain, *m* is the grain boundary mobility, and γ is the surface tension. If n < 6 (angle < 120 degrees) then the grains shrink and eventually vanish [72]. In other words, grains with less than five sides will have their faces concave inwards, while those having more than five sides will have their faces concave outwards. As a result of these curvatures, Fig. 15(b), the grains with less than six sides will tend to grow smaller, and the grains with more than six sides will tend to grow larger on the expense of grains with less than six sides [67].

Grain growth can be understood representing them topologically through soap froths and observing them as grain arrays. Evolution of the grain growth can be modeled using von Neumann-Mullins law via capillarity as undertaken by Weaire and Rivier [74]. A fixed volume of each froth container allows molecule permeation to maintain pressure in adjacent bubbles. Since the cell-walls of bubble are flexible, their geometry changes accordingly to accommodate the changes. Flexibility of cell walls (and enclosed gas) to equilibrate pressure brings soap froth in quasi-equilibrium almost immediately. But, the area of bubbles changes slowly, since the change is cell volume is limited by gas diffusion through the membrane wall. But, in polycrystalline materials the grain boundary energy varies depending on the orientation of the crystals. Additionally, transport of vacancies assist grain boundary migration is sluggish and tends to equilibrate much slowly in comparison to those of soap froth [24]. Thus, soap froth model can be utilized towards mimicking diffusion (cell air volume exchange), grain boundary migration (movement of cell walls), and achieving equilibrium.

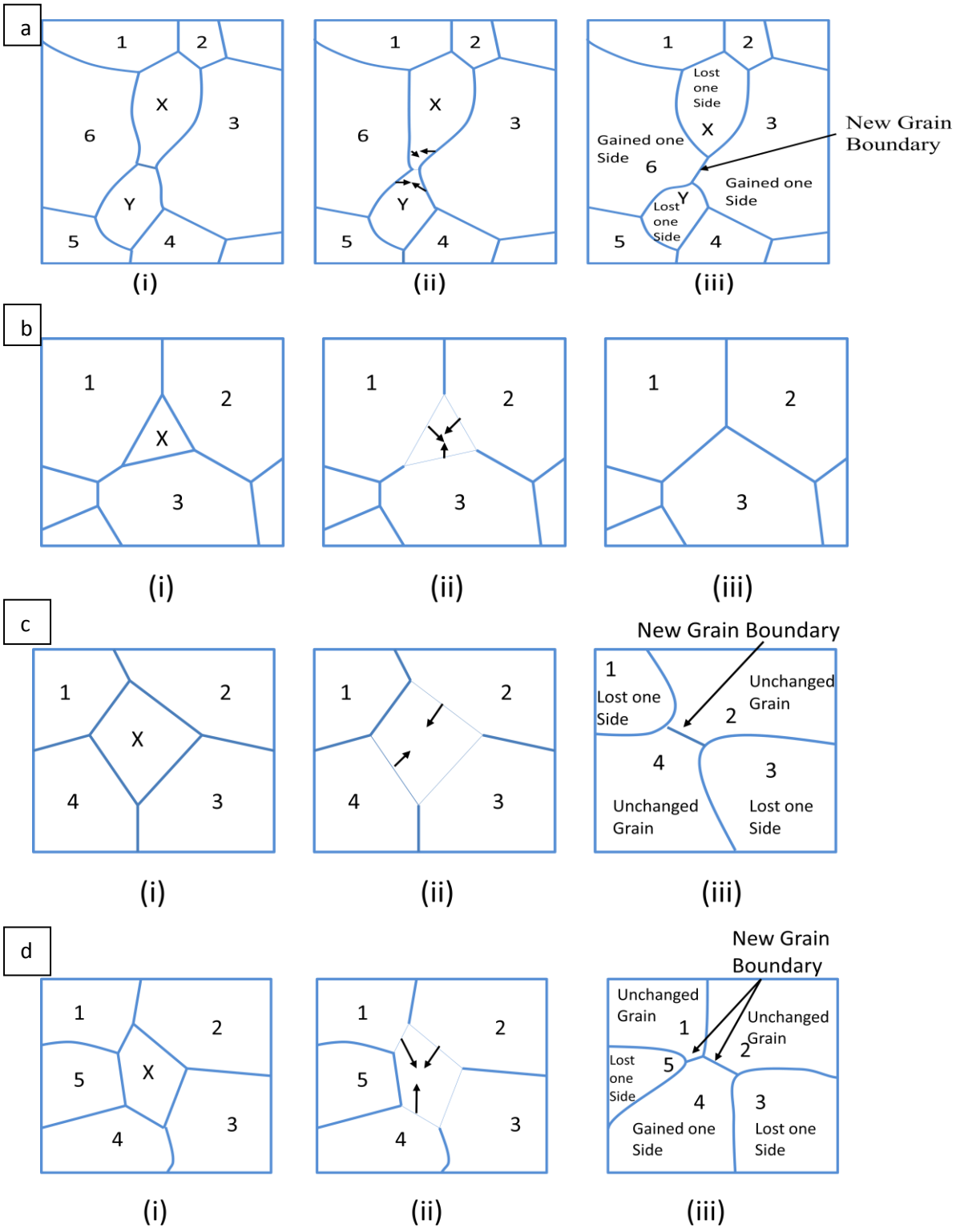

Figure 15: a) Neighbor switching mechanism among two grains. Grain annihilation in b) three-sided, c) four-sided, and d) five-sided adjoining gains. Adapted from [73].

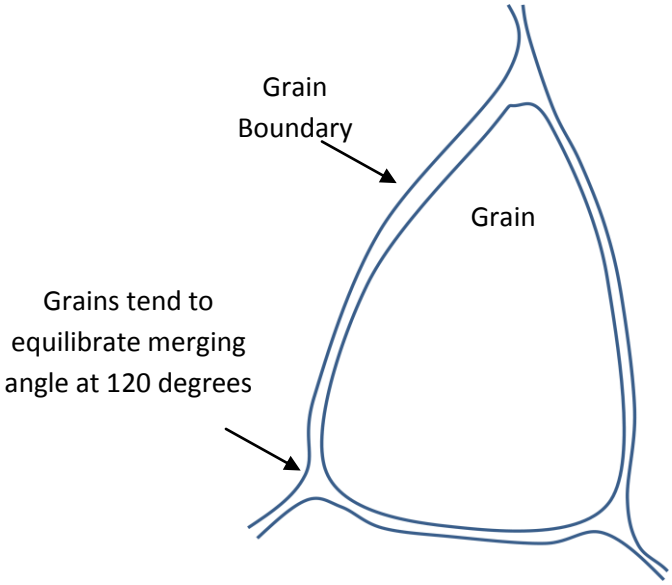

Figure 16: Typical Geometry of a Grain. Adapted from [66].

Apart from these models, grain growth mechanisms have also been defined via computer simulations [75]. Computer simulation has the advantage of graphically visualizing the procedural evolution, and attaining dynamic view in three-dimensional matrix. Computer simulation allows confirming the conceptual developed theory and eliciting newly developed features, which are difficult to predict/visualize otherwise. Computer simulations can be classified into (i) direct and (ii) statistically modeled techniques as presented in Fig. 17 [24].

Direct simulation requires constructing grains and providing initial conditions towards driving the grain boundary migration. Direct simulation can be further classified into two deterministic and probabilistic techniques, wherein deterministic technique utilizes defining subsequent configuration based on a previous configuration, whereas probabilistic technique relies on estimating a microscopic scale event probability. Conversely statistical model estimates behavior of grains (their size/shape, etc) by solving a set of governing equations without accounting for topological features. To explain grain growth various models are proposed, with two of them widely used being Monte Carlo Model and Phase Field model.

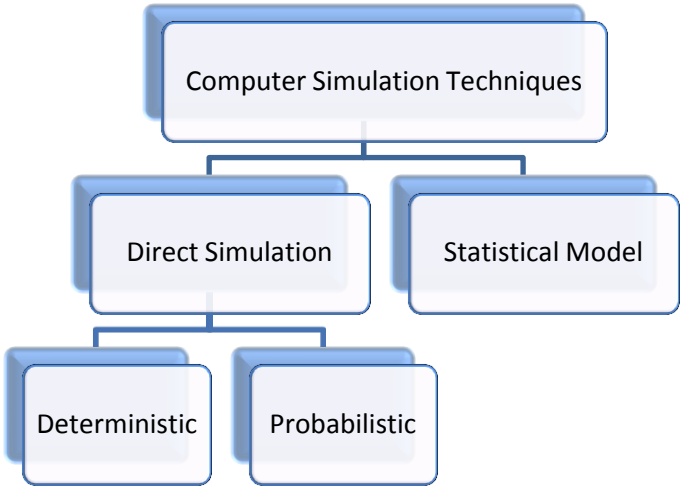

Figure 17: Classification of Computer Simulation Techniques. Adapted from [24]

Atomic interactions for the grain growth are thermodynamically simulated in the Monte Carlo technique, where a material is represented in a 2-D or 3-D matrix with specified cell volume

and each grain represented by volume and surface elements. Grains are defined by contiguous regimes of same crystallographic orientation (sharing the same directionality of crystals, as shown in Fig. 18), with the representing element storing its positional information. Organizing the initial grain structure and selecting the orientation into initial matrix, the probabilistic approach initiates the simulation [24, 75]. The main steps of the Monte Carlo algorithm are shown in the bock diagram, Fig. 19 [75-77].

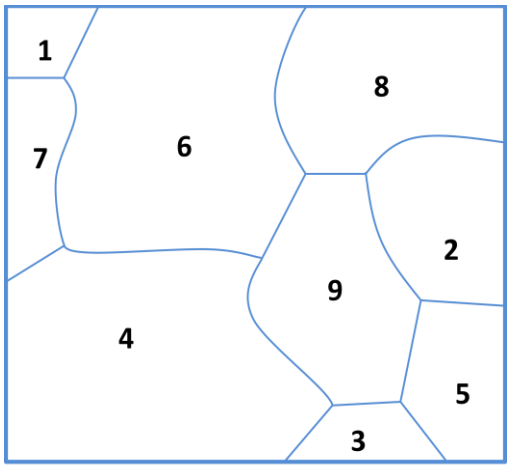

Figure 18: The schematic representation of a grain structure for Monte Carlo Method. Numbers stands for Monto Carlo number assign to particular grain. Adapted from [24].

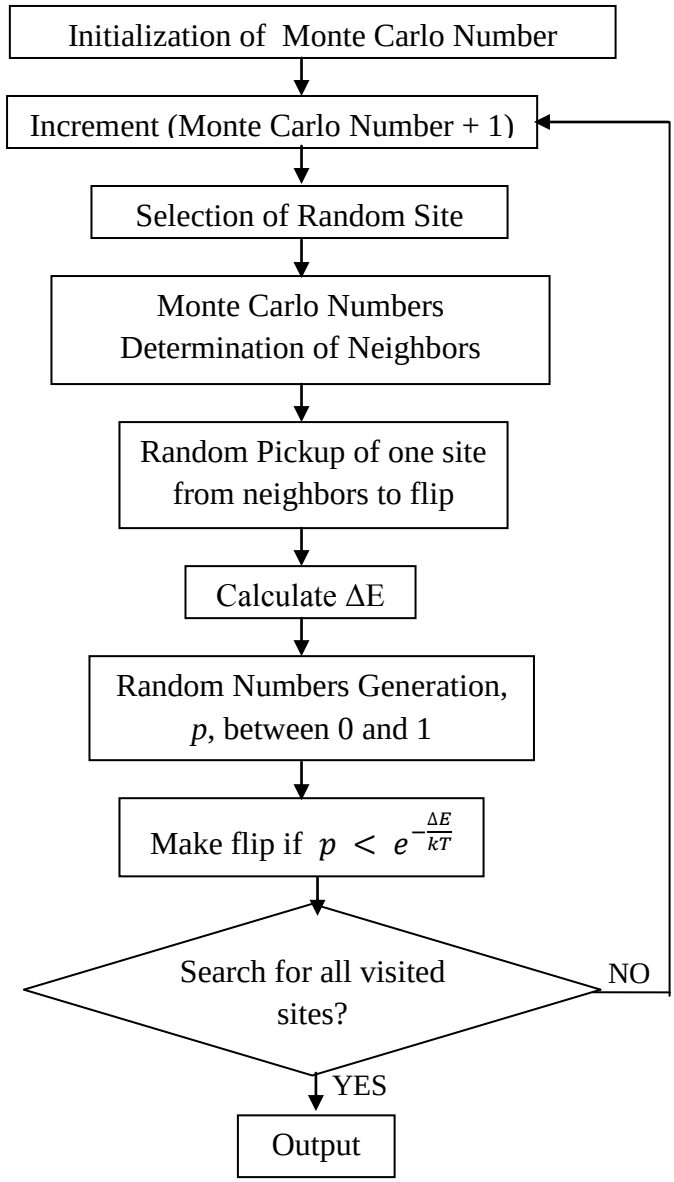

Figure 19: Algorithm for Monte Carlo model. Adapted from [75-77] .

Monte Carlo simulation brings the advantage of generalizing the model and extending it to three dimensions. But, the true prediction of grain growth results only when the pixel size is much greater than the grain size. Additionally, Monte Carlo technique fails to determine the local grain boundary curvature and can induce errors in estimating the grain boundary migration velocity [77]. Whilst in Phase Field model, a polycrystalline microstructure is described by order parameters, (such as grain orientation, size, crystallinity (***n(r)***, as shown in Fig. 20), etc.), where diffusion controlled microstructure temporally evolves via long range diffusion among grains [76, 78]. The main steps of the phase field algorithm are presented in Fig. 21 [76, 78].

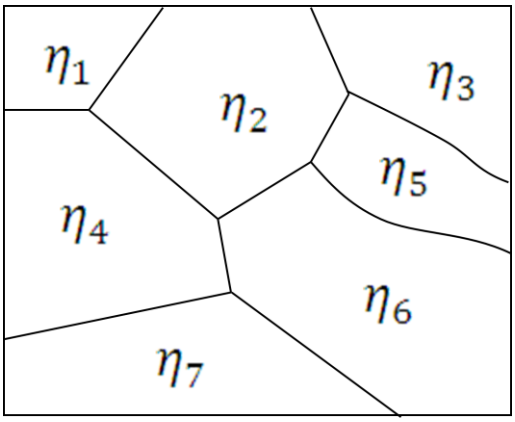

Figure 20: The schematic representation of a grain structure for Phase Field Model. Adapted from [78].

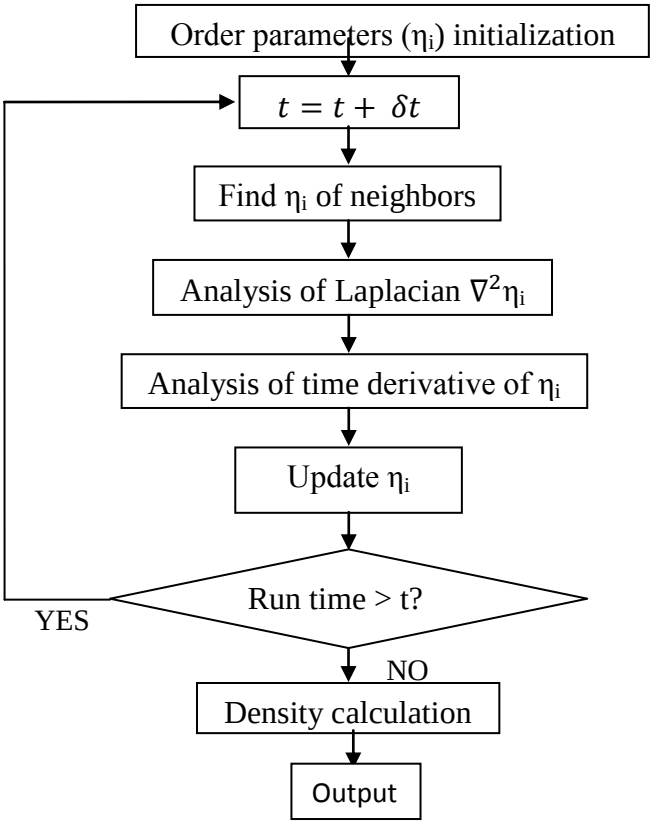

Figure 21: Algorithm for Phase Field model. Adapted from [76, 78].

When it comes to finding the dependency of grain growth on the inherent chemical composition or the kinetics related to thermal history, alloys help impeding the grain growth in comparison to those of pure metals. Aluminum, iron, zinc, pure copper show exaggerated growth along with the development of mixed grain sizes, which is not observed in brass even by straining the material before annealing. In alloys, matrix contains dispersed particles, which act as pinning junctions hindering the grain growth rate by exerting the drag force opposite to that of grain growth direction. This drag force or pinning force limits the driving force required for grain growth when the grain boundary motion has come to a complete stop.

Rios et.al. have explained the particle effect on grain growth via irreversible thermodynamic approach, which constitutes that since grain growth involves driving force overcoming the lattice

resistance, the grain boundary migration is irreversible process [79]. Hence, the increase in the total entropy results due to the grain boundary motion (i.e. $dS_i^T = dS_i^M$). However, when grain boundary encounters some obstacle (small particle), a retardation in the grain boundary mobility is observed. Therefore, an additional irreversible entropy term is generated by the bypassing of grain boundary through those particles. So the above expression can be rewritten as [79]:

$$dS_i^T = dS_i^M + dS_i^Z \quad (13)$$

Where dS_i^T is the total irreversible entropy production; dS_i^M is the irreversible entropy production due to the grain boundary motion; and dS_i^Z is the irreversible entropy production associated with bypassing such an obstacle.

Alternately, the entropy term can be converted to free energy as [79]:

$$dG^T = dG^M + dG^Z \quad (14)$$

The rate of the irreversible entropy production can be written as a product of generalized forces and the corresponding rates or generalized "fluxes" of the irreversible processes. For grain growth the total free energy is equal to the total grain boundary area times the interfacial energy per unit of area ($\frac{\gamma}{A}\frac{dA}{dt}$), whereas rate of irreversible entropy generation is the rate of change of irreversible free energy with time per unit area ($\frac{1}{A}\frac{dG^M}{dt}$). Hence the total entropy can be given as [79]:

$$\frac{\gamma}{A}\frac{dA}{dt} = \frac{1}{A}\frac{dG^M}{dt} + \frac{1}{A}\frac{dG^Z}{dt} \quad (15)$$

Form the above equation (15), it can be observed that the driving force for grain boundary motion decreases (i.e. free energy increases in presence of obstacle). Ultimately, grain growth will tend to cease when dG^M becomes zero, i.e. [79]:

$$\frac{\gamma}{A}\frac{dA}{dt} = \frac{1}{A}\frac{dG^Z}{dt} \quad (16)$$

Gil and Guilemany studied the effect of cobalt addition on grain growth kinetics in Cu-Zn-Al shape memory alloys, and reported that (i) at constant temperature grain size increases with time, and also (ii) with increase in temperature the grain growth kinetics increases [80]. But, after observing increased grain growth kinetics at higher temperature, grain growth rate gets sluggish after certain time. Then, decrease in the grain growth is reason due to increased grain size, which effectively decreases the grain boundary area, and consequently the interfacial energy decreases which accounts as driving force for the grain growth. It was also observed by Gil and Guilemany that the secondary addition of increasing cobalt in the Cu-Zn-Al alloy decreased the grain boundary mobility [80]. Hentzell et.al compared the grain growth of pure Ni with Ni-Al alloy and prepared by co-evaporation on substrates held at temperatures between 360 and 790 K. It was observed that grain size decreases with decreasing substrate temperature between 800-570 for pure Ni [81]. But, further lowering of temperatures from 570 - 480 K, the change in the grain size was only marginal depending on the change of growth mechanism. Further lowering of the substrate below 480 K displayed decrease in the grain size, but a weak dependency on the temperature was observed. By alloying Ni with Al, grain size decreased at all temperatures, which was attributed to the solution of Al in Ni (FCC) for 2-15 at.% of Al at all temperature range (360-790 K), and to the formation of alpha-Ni_3Al for 15 – 30 at.% of Al at high temperatures (above 500 K). Zhong-wei, et.al, experimentally incepted that the grain size decrease drastically with addition of solute titanium in the Al-Ti alloy till certain content (0.02% Ti, for more potent inoculation agents i.e. with TiB_2, and 0.05% Ti as less potential nuclei i.e. without TiB_2), after which the grain size become reasonably constant with further addition of alloying element [82]. Complimenting this study, similar effect of decreasing grain size was observed by their group with copper solute addition in the Al-Cu alloy [82]. Takasugi and Izumi studied recrystallization and grain growth of Co_3Ti and found that n (time exponent) was found to be less than 0.5 implying impediment of the moving grain boundary for the

expression $d = B\ t^n$, where *d* is the average grain diameter, *t* is heat treatment time and *B* is the experimental constants [83]. In other words, solutes greatly reduce the grain boundary mobility. Manor has also reported that without doping the grain size of alumina increased with sintering temperature, whereas after adding Cr_2O_3 in the Al_2O_3 matrix, inhibition of grain growth was observed [84].

The temperature dependence grain growth assumes the Arrhenius equation:

$$G = A\ exp\ (Q_G/RT) \quad (17)$$

Where, Q_G is the activation energy for the grain growth.

Cota et.al. observed that increasing the austenitizing temperature (1100 ^{0}C) resulted increased grain size as compared to that of samples austenitized at lower temperatures (900 ^{0}C) [85]. This is a result of the dissolution of a large amount of niobium carbonitrides at higher temperatures, which otherwise hinders the austenite grain growth. Higher austenitizing temperature results coarser austenite grains, and reduces the nucleation sites for ferrite formation resulting large ferritic grain size [85]. Lee et.al. stated that the tendency of abnormal grain growth increased for high-strength boron-added steel samples quenched from higher austenitizing temperatures [86].

4. Solute Drag Effect Affecting Kinetics of Grain Boundary Mobility:

Solute drag is a mathematically well developed theory for explaining the reason for slow growth rate in doped ceramic materials when compared to that in undoped ones. Solute drag theory also explains the reason behind grain growth exponent becoming greater than two. Conversely, it is well established that some dopants enhance grain boundary mobility (such as calcium doping in alumina), while some reduce it (such as magnesia doping in alumina). Magnesia prevents abnormal grain growth in alumina due to the drag that the magnesia solute exerts on the alumina grain boundary. Thus, slow grain growth is observed in magnesia doped alumina, when compared to that of undoped alumina. Thus, calcia doping should produce a stronger drag effect owing to its heavier nature in comparison to magnesium. But, contrastingly, calcia has shown to enhance the grain boundary mobility as compared to that of undoped alumina. Correspondingly, it becomes imperative to device solute drag effects on the microstructural development and affecting the resulting properties.

Structural transitions in alumina are experimentally defined by complexions, which are responsible for the enhanced or impeded grain mobility in presence of doped particles (such as magnesia and calcia) [87]. Grain boundary mobility is a function of the interfacial sub-monolayer adsorption (in magnesia doped alumina) to show reduced mobility, whereas bi-layer adsorption (in calcia doped alumina) to show enhanced grain mobility. Hence the transitions or complexions occurring at the grain boundary are the cause of discrepancy in determining grain mobility in presence of dopants. However, how actually the calcium cations assist the grain boundary mobility while reducing drag force is still unclear.

Cahn has described the grain growth kinetic being affected by solute by a drag force F, for a range of grain boundary velocities [88]:

$$F = \frac{\alpha C_\infty \vartheta_b}{1+\beta^2 {\vartheta_b}^2} \quad (18)$$

where ϑ_b is the grain boundary velocity and C_∞ is the concentration of the solute in the bulk grain

$$\alpha = 4N_v KT \int_{-\infty}^{+\infty} \frac{sinh^2\left[\frac{U(x)}{2KT}\right]}{D_b(x)} dx \quad (19)$$

and

$$\beta = \left[\frac{\alpha}{\frac{N_v}{KT}\int_{-\infty}^{+\infty}\left(\frac{du}{dx}\right)^2 D_b(x)dx}\right]^{1/2} \quad (20)$$

where U is an interaction potential between the boundary and the solute, K is Boltzmann's constant, D_b is the diffusion coefficient of the solute, N_v is the number of host atoms per unit volume, x is distance from the grain-boundary and T is temperature. From which, the grain-boundary velocity under solute drag is given as [89]:

$$\vartheta_b = \frac{M^{\circ}F}{1+4N_v\Omega QC_{\infty}} \quad (21)$$

where Q is a partition coefficient of the dopant distribution between the bulk and the grain boundary, M° is the intrinsic grain-boundary mobility and Ω is the atomic volume of the solute [89].

The drag factor is the empirically determined measure of the solute drag force and is defined as the derivative of mobility with respect to grain size, thus, describing the drag effect of the solute. It is evident that for direct comparison, theoretically predicted drag factors of different dopants need to be verification after their comparison with the normalized drag factors experimentally observed. Dillon et al. have confirmed that the reduction in the grain growth rate due to magnesia and other rare earth dopants in alumina matrix arises due to solute drag from their intrinsic mobility [89]. Herein, dopants tend to segregate at the core of the grain boundary unlike classical solute drag models, where the drag effect is obtained from the solute in the near-boundary lattice. In the case of grain boundaries which have their mobilities enhanced relative to the pure metal, again, solute drag factor can be employed to understand the role of drag [89].

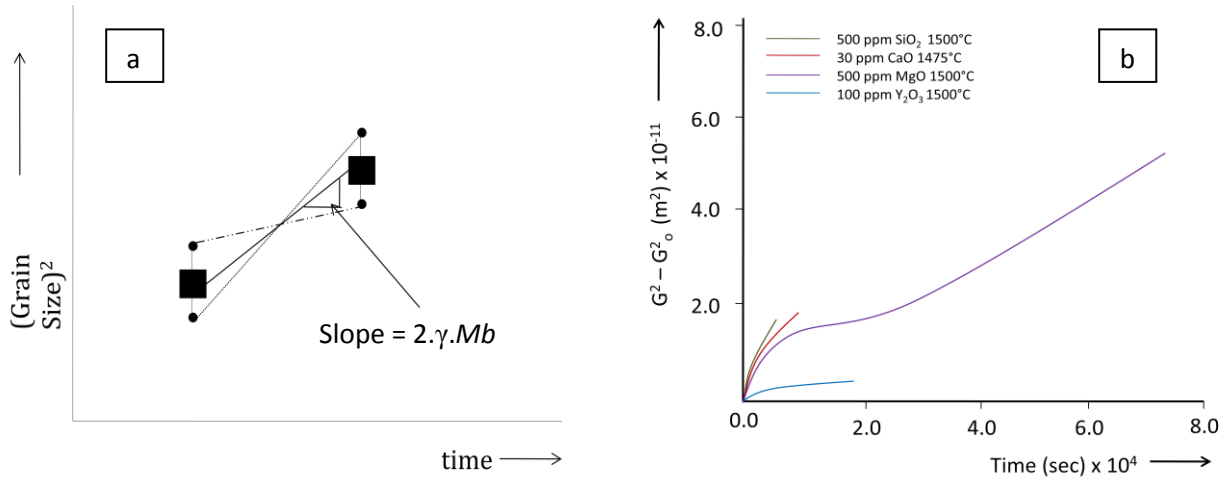

Figure 22: (a) Calculations errors arise from the difference in the slopes of grain sizes at various times for grain boundary mobility evaluation, and b) Effect of dopants in alumnia are presented, showing parabolic kinetic (n = 2) with dopants of 500 ppm magnesia, 500 ppm silica, 30 ppm calcia, and 100 ppm yttria in alumina matrix at a temperature of ~1500 ^{0}C. Solute drag is evident as points deviate from parabolic kinetics. Adapted with permission from [89].

Reduction in the grain boundary mobility is caused by grain boundary excess solute Γ assuming there are no solute-solute interactions with solute inducing drag on the grain boundary mobility, M_b [89].

$$\frac{dM_b}{d\Gamma} = -H \quad (22)$$

where H represents the relative drag force, and can be replace by a constant C. The calculated grain-boundary solute excess is given as [88]:

$$\Gamma = \frac{XG}{3\Omega} \quad (23)$$

where G is the grain size and Xe is the concentration of dopant or impurities above the solubility limit. Consequently, the kinetics of grain growth is given by [89]:

$$G^n - {G_0}^n = Kt \quad (24)$$

where t is the time, n the grain growth exponent and K the grain growth constant. Depending on chemistry and sintering conditions n varies between 2 and 6, and n > 4 has been observed in doped aluminas. Grain growth kinetics for n=2 is seen in Fig. 22(b). Thus, solute drag deviation from linearity can be ascribed to follow the equation [89]:

$$\frac{dM_b}{dG} = -C \quad (25)$$

where C is the drag factor (a constant) and M_b is the grain boundary mobility [89].

Grain boundary mobility versus grain size data assuming that the grain boundary energy was 0.3 J/m^2 is shown in Fig. 23 [88]. From this it is seen that the measured grain growth exponent will be a function of the grain size range over which the measurement was performed and will continuously increase with decreasing grain size. Due to increase in the grain boundary excess the solute drag force described by Cahn and Hilbert increases with increasing grain size [89].

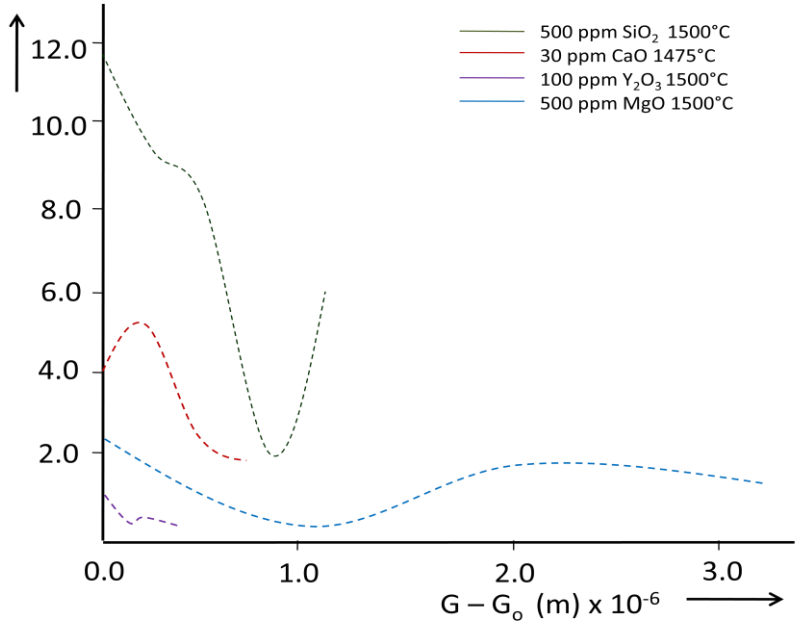

Figure 23: Mobility versus grain size plot for 500 ppm magnesia-doped alumia, 500 ppm silica-doped alumina, 30 ppm calcia-doped alumina, and 100 ppm silica yttria-doped alumina at 1500 ^{0}C. Adapted with permission from [89].

A linear decrease in the grain boundary mobility with increasing grain size corresponds well with the linear increase in the solute excess available at grain boundary (with increasing grain size). This relation is independent of chemistry and morphology. The grain boundary mobility when grain size is zero becomes the mobility in the absence of solute drag. This analogy is imperative since as the grain size approaches zero the grain boundary excess concentration also approaches zero, as the grain boundary area becomes infinite. Thus, it becomes possible to extrapolate to the true intrinsic mobility of the material for undoped material or material that is growing by intrinsic mechanism as shown for few cases in Fig. 24 a. From Fig. 24 a it is evident that solute drag is the mechanism for reduction of grain boundary mobility for yttria, lanthana and magnesia dopants in alumina matrix.

Evidently, the grain boundary mobility decrease with decreasing temperatures is also presented in figs. 24 b. The combined effect of reduction in temperature and enhanced concentration of reinforcement to impede grain boundary mobility is presented in Fig. 24 b.

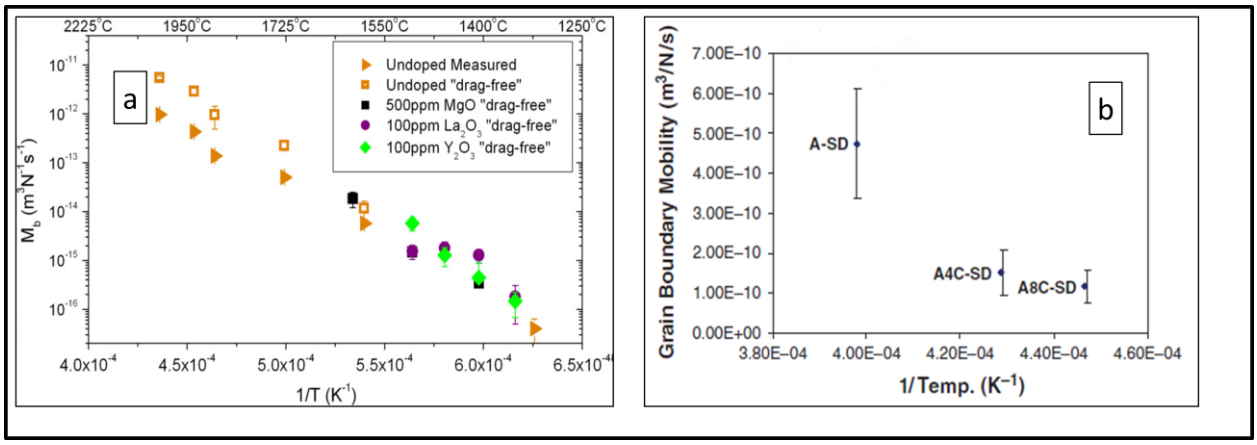

Figure 24: (a) The zero grain size mobility (i.e. ‘‘drag-free”) for undoped and some doped aluminas, along with the measured data for undoped alumina Reprinted with permission from [89] and (b) Reduction in the grain boundary mobility showing grain boundary pinning due to CNT. Reprinted with permission from [90].

The solute drag factor is affected by the concentration of the dopant relative to the their solubility limit in alumina, thus normalizing the drag factor by composition of dopant becomes difficult. Also grain boundary structural transitions produced by some dopants enhance mobility relative to undoped material and hence the drag-relieving effects will vary significantly depending on the mechanism. To compensate for the fact that normal grain growth may occur by: (i) different type of complexion and (ii) effect of different dopant levels and solubility, the drag factor may be normalized C_n, to the initial measured mobility, M^i as [89]

$$C_n = \frac{C}{M^i} \tag{26}$$

Normalized drag factor as a function of temperature for various aluminas is already shown in Fig. 24, but the normalized drag factor, Fig. 25, generally increases with dopant ionic radii. A drag force is imposed on the grain-boundary by dopants, such as silica and calcia, which enhance grain growth kinetics by inducing a grain-boundary complexion transition. Even though the grain-boundary mobility of magnesia-doped alumina is lower than that of calcia doped alumina, calcia produces a stronger drag force than magnesia. So, when it comes to dictating the grain boundary mobility, it is the grain boundary complexion which dominates over the solute drag effect. At the same time, different grain-boundary complexions essentially have different solute profiles, and allow different levels of disorder in their core. For the breakeven velocity for changing the complexion from one to another, forces increase with increasing grain-boundary velocity as predicted by classical solute drag theory. But, these theories are not confirmed for alumina, since measured normalized drag factor have large error associated with it and hence temperature dependence of solute drag factor on affecting grain boundary mobility cannot be predicted.

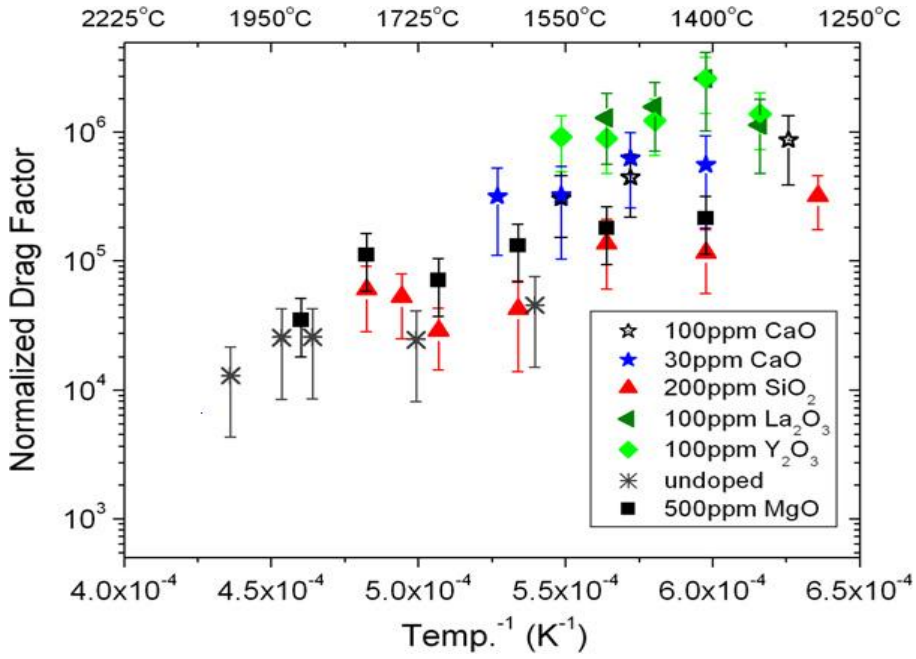

Figure 25: Normalized drag factor for various doped aluminas with undoped alumina for comparison. Reprinted with permission from [89].

Interfaces are of primitive importance in deciding material utility or failure. Despite their small effective volume fractions, interfaces and grain boundaries promote rapid transport relative to the bulk. Thus, being able to manipulate interface transport either to (i) speed up grain boundary transport to grow single crystals from polycrystals etc. or (ii) slow down interface movement to suppress abnormal grain growth will provide command to materials scientist in engineering ultra-high-strength materials etc. Previously many techniques like controlling interfacial area, applied forces, geometry, temperature, and interface chemistry have been used for kinetic engineering [87]. Since interfaces have many characteristics which can affect transport kinetics interface complexion is suitable for kinetics engineering as reported by Dillon et al [87]. Features that can be differentiated (such sites, geometry, or structure) are specified by particular sets of intensive thermodynamic variables (P, T, μ_i), interface inclinations and misorientations (for grain-boundaries) $\Delta\Theta_i$. They have associated equilibrium quantities like excess volume, entropy and adsorption in addition to equilibrium thickness and are similar to thermodynamic bulk phases. Two different boundaries possessing the same complexion will not have the same exact atomistic structure, but rather will have similar characteristic equilibrium thermodynamic quantities. These equilibrium features have been designated as interface complexions by Dillon et al [87].

Internal interfaces and their environmental conditions are difficult to control or measure when compared to those of crystalline-free surfaces. Additionally, crystallographic misorientation introduces three additional geometrical degrees of freedom compared to those of free surfaces. Thus, changes in complexions of internal interfaces can be observed by measuring an interface dependent property as a function of critical variables. A change in kinetics or the property may signify change in complexion which can be verified ex situ.

Alumina has six complexions, wherein transitions can affect atom transport by many orders of magnitude. The role of magnesia in preventing AGG in alumina, and role of calcia in inducing AGG in alumina may be understood with the help of interface complexions. The role of complexions on transport can be evaluated by grain growth kinetics since they can be measured over wide range of conditions and are easily quantifiable. The driving force for the growth of the abnormal grains is the grain boundary curvature which is related to the grain size of the normal grains. Fig. 26 shows microstructures of some samples with varying grain sizes arising out of

different complexions. The grain boundary energy is assumed to be constant as 0.3 J/m^2. Grain growth rate of an abnormal grain is given by [87]:

$$\frac{dG_A}{dt} = \frac{\alpha\gamma M_b}{G_N} = \frac{k_A}{G_N} \quad (27)$$

where M_b is the mobility of the abnormal grain, G_A areis the grain size of the abnormal grains and G_N is the grain size of normal grains, at any time *t*, and γ is the grain boundary energy. For normal grains, grain growth can be approximated as [87]:

$$G_N = k_N{}^{\frac{1}{n}} t^{\frac{1}{n}} \quad (28)$$

and combining with equation 24 and integrating we get the equation for growth of an abnormal grain into a matrix of growing normal grains [87]:

$$G_A - G_{A0} = \frac{k_A}{k_N{}^{\frac{1}{n}}} \left(\frac{n}{n-1}\right) t^{\left(\frac{n-1}{n}\right)} \quad (29)$$

It is to be mentioned that the error resulting due to this approximation is less than the experimentally calculated error. To get the grain boundary mobility, *n* is taken to be 2 (though parabolic kinetics do not give best fit for normal grain growth data since *n*>2 due to drag effect). Thus grain boundary mobility is decreasing with increasing grain size but the decrease is smaller than the limit imposed by experimental errors hence taking *n* to be 2 is more or less reasonable.

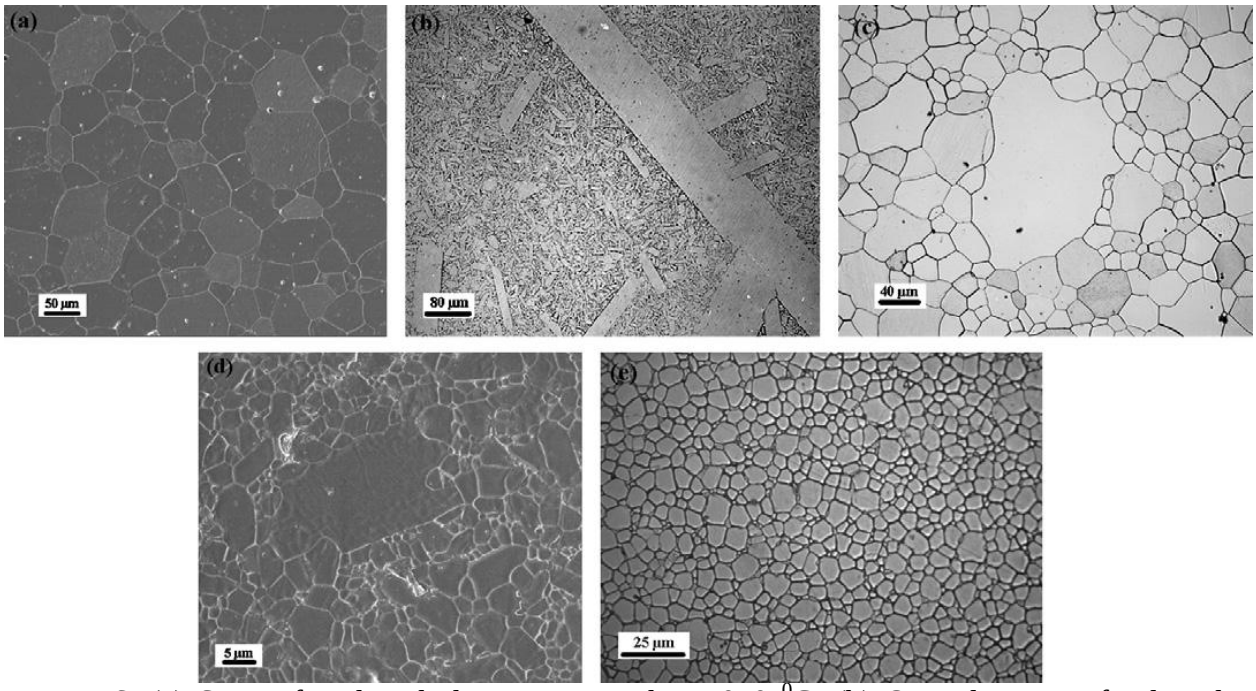

Figure 26: (a) SEM of undoped alumina sintered at 2020 ^{0}C; (b) Optical image of calcia-doped alumina sintered at 1675 ^{0}C; (c) Optical image of silica-doped alumina sintered at 1750 ^{0}C; (d) SEM of neodymia-doped alumina sintered at 1400 ^{0}C; and (e) Optical image of magnesia-doped alumina sintered at 1600 ^{0}C. Reprinted with permission from [87].

Grain boundary mobility changes with temperature as shown in Fig. 24 b. Alumina is represented by type II which serves as the reference. Six different types of kinetic behaviour can be distinctly identified, where both normal and abnormal grains have been found to co-exist. Neodymia doped alumina shows normal grains of type I and abnormal grains of type III while silica doped alumina at low temperatures shows normal grains of type III and abnormal grains of type IV. High resolution electron microscopy can be used to validate the existence of these six grain boundary phases as shown in Fig. 27. Intergranular films are not seen in complexions I, II and III by HRTEM while they are seen in IV, V and VI. Complexions I, II and III can be differentiated using

atomic-resolution HAADF-STEM (fig. 27). Presence of neodymium is confirmed from the bright spots seen in HAADF-STEM images. It is difficult to distinguish between complexions I, II and III. Type V complexion depicting intergranular glassy film has also been reported by Subramaniam et.al. [91]. However, the grain boundary transitions show certain traits like (also see Fig. 28):

(i) sub-monolayer adsorption in complexion I,
(ii) no segregation in complexion II,
(iii) bilayer adsorption with boundary width ~0.35 nm in complexion III, while
(iv) complexion IV shows a 0.6 nm disordered layer (multi-layer adsorption),
(v) complexion V shows a ~1.5 nm intergranular film, and
(vi) complexion VI contains a thicker wetting intergranular film that may have arbitrary thickness.

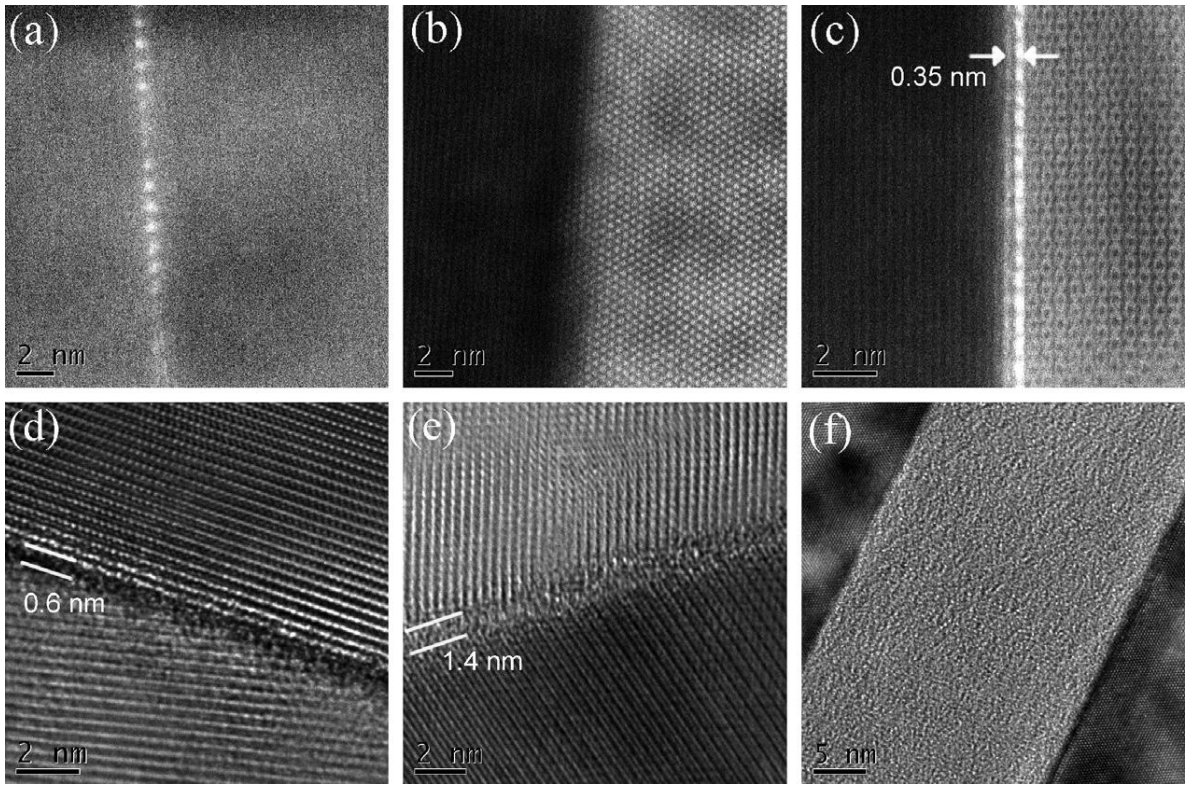

Figure 27: High-angle annular dark-field scanning transmission electron micrographs of (a) complexion I, (b) complexion II and (c) complexion III, and high resolution transmission electron micrographs of (d) complexion IV, (e) complexion V and (f) complexion VI. Reprinted with permission from [87].

The mobilities of the six different types of kinetic behaviors seen in alumina range over three orders of magnitude and their corresponding mobilities correlate with different chemistries and different dopant levels. Contrastingly, silica-doped alumina grains are equiaxed and curved, while calcia-doped grains are mostly elongated and faceted. The SiO_2 doped Al_2O_3 undergoes a transition between 1400 - 1500 ^{0}C, where abnormal grains consume all of the normal grains to establish distribution similar to that of a *normal grain growth*. Thus, complexions affect the kinetic mobility and distribution of grain sizes.

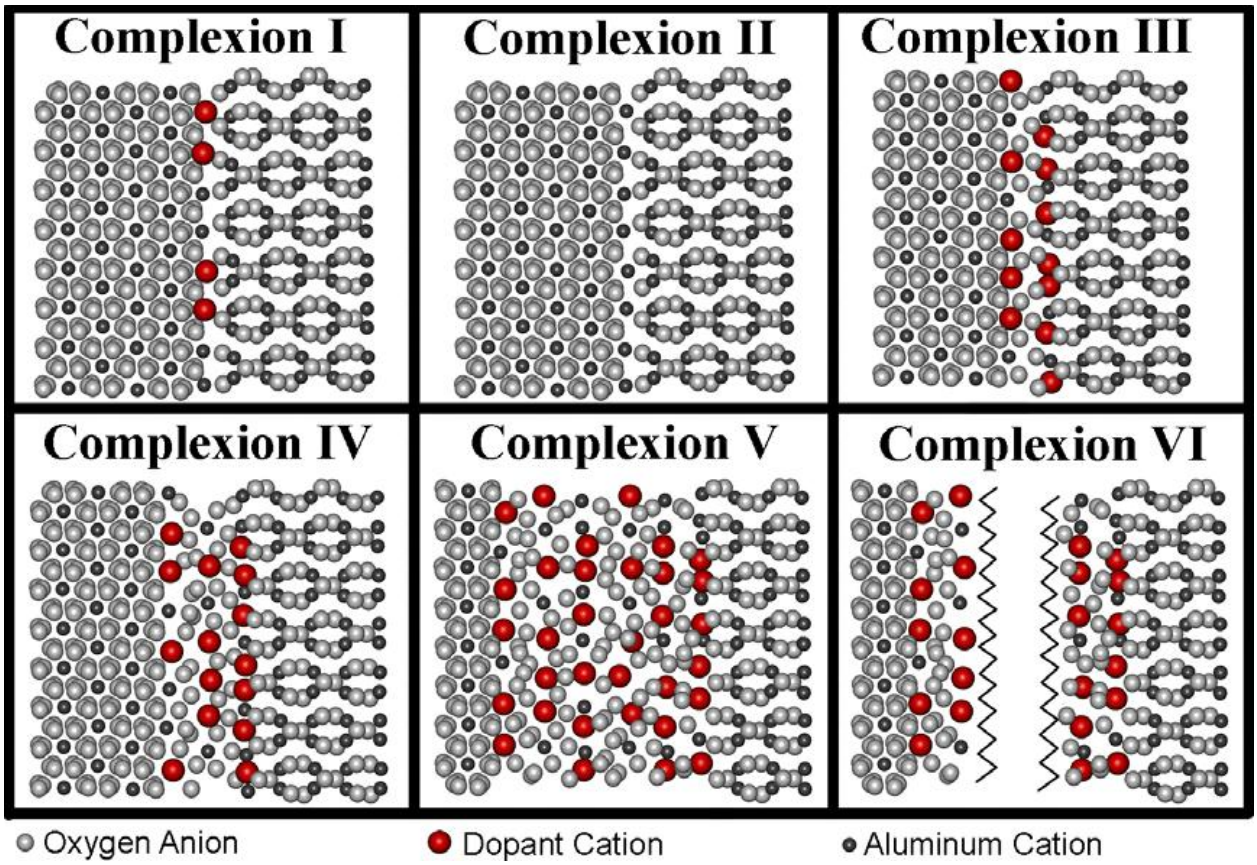

Figure 28: Grain boundary complexions; schematic: (I) sub-monolayer adsorption; (II) the ‘‘clean’’ grain boundary; (III) bilayer adsorption; (IV) multi-layer adsorption; (V) amorphous intergranular film of equilibrium thickness; (VI) wetting film. Reprinted with permission from [87].

The atomic-disorder in the grain boundary leads to entropic effects, which affect the kinetics of grain mobility while keeping the enthalpy constant for different complexions. Thus, the exponential prefactor for grain growth is governed by complexions while the activation energy arising from the interface barrier remains constant for differently doped aluminas. Which in turn means that transport kinetics of alumina can be controlled by controlling the thermal history, processing-conditions, and chemistry of dopant in alumina. But, the stability of a complexion to control the grain boundary mobility can also get affected by grain misorientations, which means that two different grain boundaries between same phases can have two different complexions.

Interfaces derive the transitions at the grain boundary governed by the phase diagram and the driving force leading to eventual equilibrium. Representation of these complexion maps eliciting interfacial reactions through a phase diagram can be of extreme importance when it comes to their kinetic engineering [92].

Dillon et al. [87] has modified Cahn’s wetting model for predicting crystallographic misorientations in the equilibrium phase diagrams, fig. 29. These misorientations affect the grain boundary interfacial thickness, degree of disorder and composition of a dynamically equilibrated interface, i.e. generation of various complexions [87]. A prototype phase diagram developed of binary alloy complexion was developed by Dillon et. al., which produced three boundary associated parameters of: (i) grain boundary thickness, (ii) grain boundary structural disorder, and (iii) adsorption (or chemistry) under equilibrium. It was confirmed that the stability of a particular complexion was found to be dependent on the chemistry, grain boundary crystallography and temperature. Consequently, the complexions of (a) an ordered grain boundary with low segregation (a coarse-grained description of complexions I–IV, which cannot be distinguished from each other in the model), (b) a non-wetting intergranular amorphous film (complexion V), and (iii) a wetting liquid film (complexion VI) were identified [87]. “A first-order transition from the ordered state to intergranular film can occur at sub-eutectic and sub solidus temperatures for grain boundary with

large misorientation energy. Complexion II only exists in pure Al_2O_3. Two hypothesized complexion coexistence (complexions I, III and IV) are based on the multi-layer adsorption at grain boundaries and surfaces. The complexion transition from V to VI happens when the system approaches the eutectic line from the two phase region or the solidus line from the single phase region. For special boundaries (e.g. boundaries containing the basal plane) with less misorientation energy, the transitions to complexions V and VI are less likely." [87].

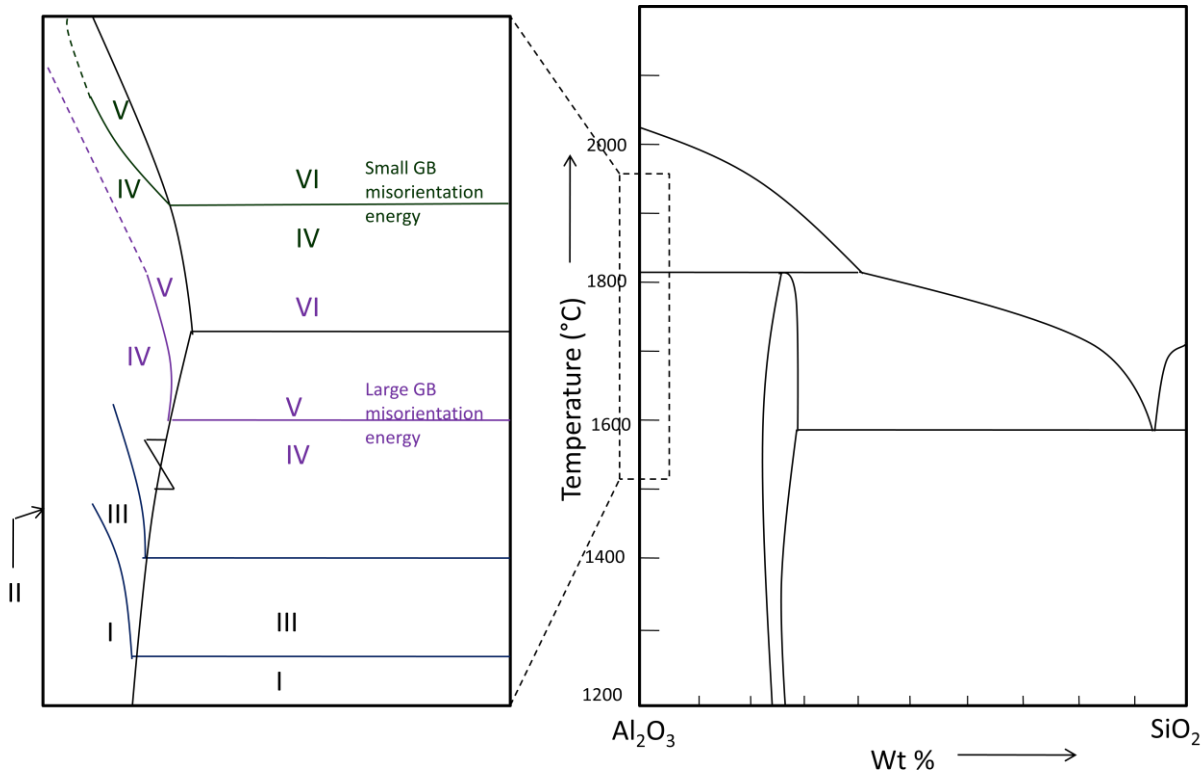

Figure 29: (a) Schematic of a complexion diagram for a binary eutectic e.g. Al_2O_3–SiO_2, whose bulk phase diagram is shown in (b). Various stable complexions are labeled for comparison. Reprinted with permission from [87].

Any single complexion does not define the abnormal grain growth (AGG), albeit results due to coexistence two or more different complexions, Fig. 30. For example presence of calcia and magnesia result formation of 1-2 nm intergranular layer (Complexion 4) resulting an abnormal increase in the grain growth is surrounded by finer grains obeying lower complexions of hindered grain mobility. Dopant concentration can decide the grain growth mobility at various locations and therefore, grains (or grain growth as such) cannot be held responsible for defining absolute kinetics of grain boundary mobility. Complexions explain certain discrepancies such as impeded or enhanced grain growth by various dopants and occurrence of AGG in the absence of intergranular film. In addition, amorphous interlayers (as in complexion V) result wear grain boundaries, which assist in enhancing fracture toughness via crack-deflection at the grain boundary interface. It can be concluded that thermodynamics does not predict the grain boundary structure, though grain boundary mobilities have a direct dependence on the temperature. It is also observed by Dillon et.al., that extrinsic activation can be promoted by inducing grain boundary disorder and thus activating abnormal grain growth (AGG) [93]. Further, complexions stable at higher temperatures may not be observed upon cooling, and lower order complexions are hard to distinguish even by HRTEM. Though HAADF, atomic resolution Z-contrast STEM etc., do resolve among lower order complexions, but there have been only limited studies on identifying theses interfaces.

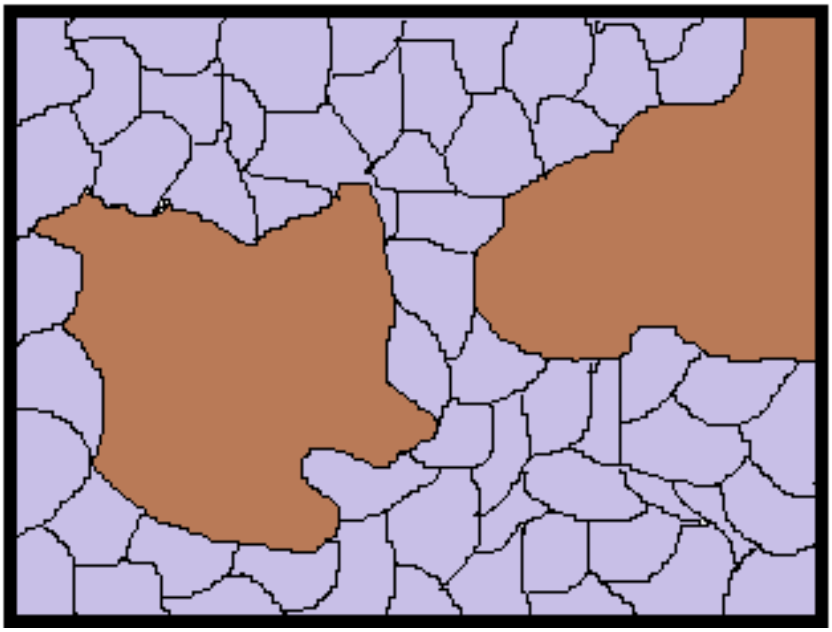

Figure 30: Schematic showing AGG due to coexistence of two different complexions (I (purple) and IV (brown)) with different mobilities. Adapted from [87].

Intergranular glassy films (IGF) have been observed at dissimilar ceramic interfaces and at metal-ceramic interfaces and are generally 0.5-2 nm thick [90]. IGFs usually enhance grain boundary transport phenomena, but even absence of IGF or grain boundaries may assist grain boundary mobility. Hence, grain growth kinetics of grain boundary interface can be compared to that of lattice-gas model, where force balances elicit equilibrium across the boundaries between different cells [94]. Means of looking at the interfaces and classifying them based on misorientation, order, phases, and chemistry is presented in Fig. 31.

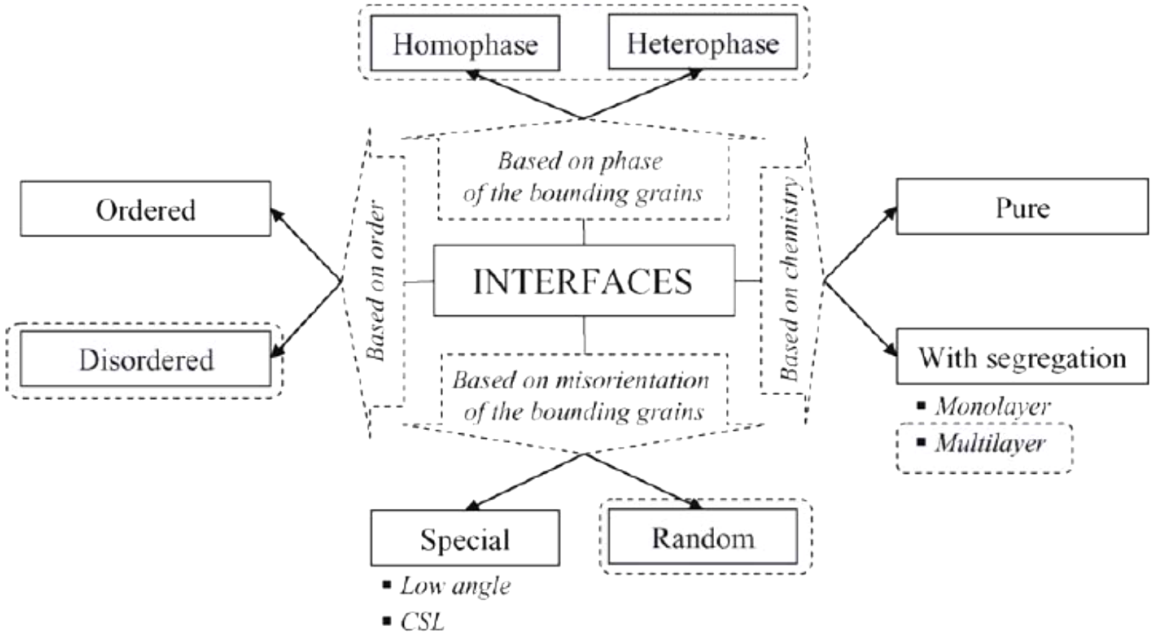

Fig. 31: Classification of internal interfaces in materials. Reprinted with permission from [91].

In *sub-monolayer* adsorption the grain boundaries do not contain an intergranular film and the dopant cations segregate at large sites within the grain boundary core. *Supersaturated* boundaries in which the dopant has not yet precipitated may lead to AGG. Due to *multilayer*

adsorption abnormal grain boundaries in the fast growth direction contain a 0.6 nm intergranular film formed below ~1590 ^{0}C and the boundary contains three layers of cation adsorption. Between ~1590 to 1700 ^{0}C the AGG that occurs contains a pre-wetting or pre-melting intergranular film which was believed to be 1 to 2 nm thick and in alumina it is found to vary between 1.3 and 1.4 nm and is called *thin film*. AGG at temperature greater than 1700 ^{0}C has a thick variable grain boundary film called *true wetting film* due to its arbitrary thickness (~5-20 nm).

Atomically rough grain boundaries containing an IGF of 10-20 nm thickness have been reported by Dillon and Harmer [95] to showcase highest mobility in single crystal conversion experiments in abnormal grains in alumina [96]. Intergranular fracture rather than transgranular fracture is seen in silicon nitride due to IGFs thus enhancing its toughness while reducing strength simultaneously. Reduction in creep rate by two orders of magnitude due to IGFs has been observed in alumina doped with certain rare earths [97, 98] but this effect disappears at a critical temperature and may be associated with grain boundary structural transitions. Grain boundary structural changes and formation of IGFs in particular may affect oxygen diffusion [100] hence they are important in thermal barrier coatings.

Three areas, abnormal grains of near normal size, normal grains and abnormal grains growing in the direction of the gradient can be clearly made out from Fig. 32. This type of figure has also been reported by other authors earlier [100].

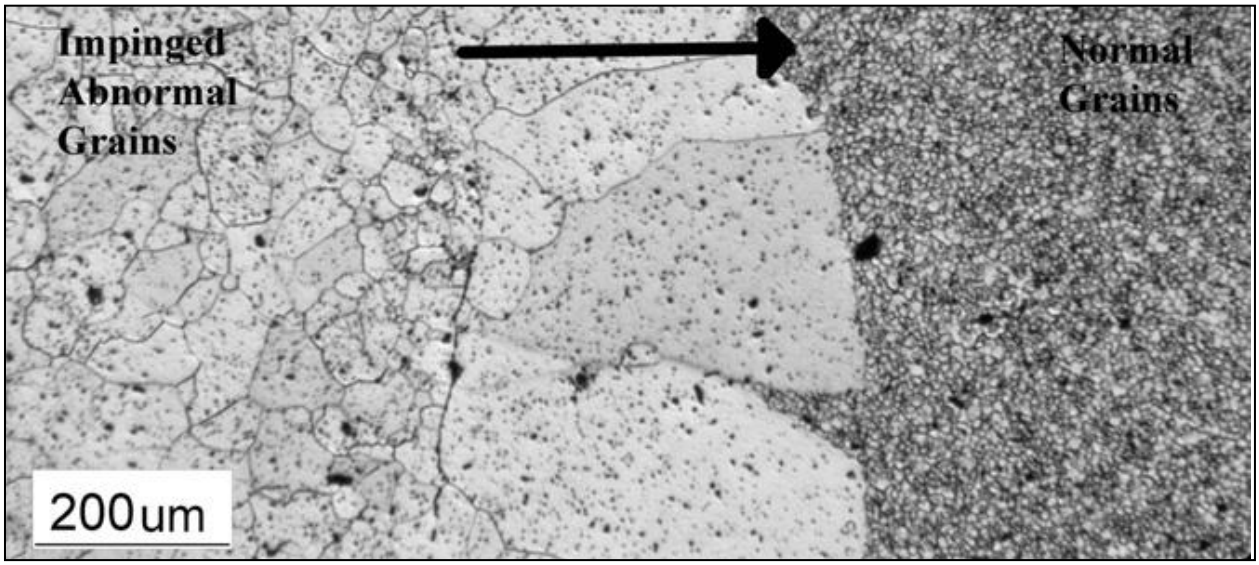

Figure 32: Optical image showing gradient microstructure and abnormal grain growth direction in a sample sintered at 1700 ^{0}C for 15 min. Reprinted with permission from [93].

AGG is stimulated and grain boundary mobility increased by sintering of the 0.5 nm thick disordered layer that is formed at the grain boundaries by Y and Si doping in alumina as shown by MacLaren et al. This grain boundary layer could be a transition phase in the crystalline to amorphous change or [101] could be a layer of adsorbate [102] which is more appropriate. Impure and doped alumina (with silica and calcia especially) has shown AGG in non wetting grain boundary films with equilibrium thickness in 1- 2nm range. [103]. These films have been distinguished from the thin IGF ~0.6 nm by Dillon and Harmer [104]. Multilayer adsorption has been reported and correlated to increase in grain boundary mobility by Dillon and Harmer [104] in alumina doped with Nd and annealed at 1800 ˚C. AGG is also stimulated by supersaturation of Nd in grain boundaries at 1450 ˚C with certain combinations of grain size and dopant concentration as shown by Wang et al. [105].

Abnormal grain growth (AGG) is promoted at high sintering temperatures, which become essential for complete densification of ceramics. AGG is stimulated and grain boundary mobility increases by sintering by Y- and Si- doping in alumina forming a 0.5 nm thick disordered layer at the grain boundaries [101]. This grain boundary layer could be a transition phase in the crystalline

to amorphous change or [101] could be a layer of adsorbate [102] which is more appropriate. Impure and doped alumina (with silica and calcia especially) has shown AGG in non wetting grain boundary films with equilibrium thickness in 1- 2nm range [103]. These films have been distinguished from the thin IGF ~0.6 nm by Dillon and Harmer [104]. Multilayer adsorption has been reported and correlated to increase in grain boundary mobility by Dillon and Harmer [104] in alumina doped with Nd and annealed at 1800 ˚C. AGG is also stimulated by supersaturation of Nd in grain boundaries at 1450 ˚C with certain combinations of grain size and dopant concentration as shown by Wang et al. [105].

Secondary sintering additives act as barriers for grain growth, and impede grain growth [106]. Since carbon nanotubes (CNTs) reinforcements in alumina matrix has shown enhanced mechanical properties (improvement in fracture toughness by three times), it becomes essential to evaluate dependence of the grain growth on the initial grain size, thermal history experienced by grain (temperature and dwell time) in presence and absence of secondary reinforcement (carbon nanotubes, CNTs) [90]. Since the experimental parameters can provide the details of processing conditions (i.e. temperature, and time of processing), and the resulting grain size data can be evaluated through consequent analysis, a direct comparison can be evolved to comment on the role of the grain size and secondary reinforcements in impeding grain growth. The grain boundary mobility (M_b) of Al_2O_3 with and without carbon nanotubes (CNTs) has been compared using the following formula [89]:

$$M_b = \frac{V}{2\gamma}\left(\frac{1}{G_f} - \frac{1}{G_i}\right)^{-1} \tag{30}$$

where V is the average velocity of grain growth (m/s), G_f and G_i are the final and initial grain sizes (m) of samples before and after thermal processing (plasma-spraying and hot-isostatic pressing (HIPing) respectively, and γ is the grain boundary energy of Al_2O_3 (taken as 0.3 J/m^2).

First step was to develop a process map wherein the role of CNT dispersion in altering the thermal exposure to the splats during plasma spraying was correlated [107]. Herein the interdependence of initial powder feedstock, plasma parameters, and processing conditions are the main parameters, Fig. 33, that control the thermal and kinetic profile experienced by powders to form a coating on a given substrate. Therefore four sets of powder feedstocks were prepared, namely (i) Al_2O_3 (A-SD), (ii) Al_2O_3 with 4 wt.% agglomerated CNTs (A4C-B), (iii) Al_2O_3 with 4 wt.% dispersed CNTs (A4C-SD), and (iv) Al_2O_3 with 8 wt.% dispersed CNTs (A8C-SD). These powders were plasma sprayed onto a steel substrate to develop thick coatings of Al_2O_3 with varying CNT contents differentiated by their content and dispersion. The overall effect in the reduction of thermal damage and kinetic profile observed by powder particles during plasma spraying is represented in Fig. 34.

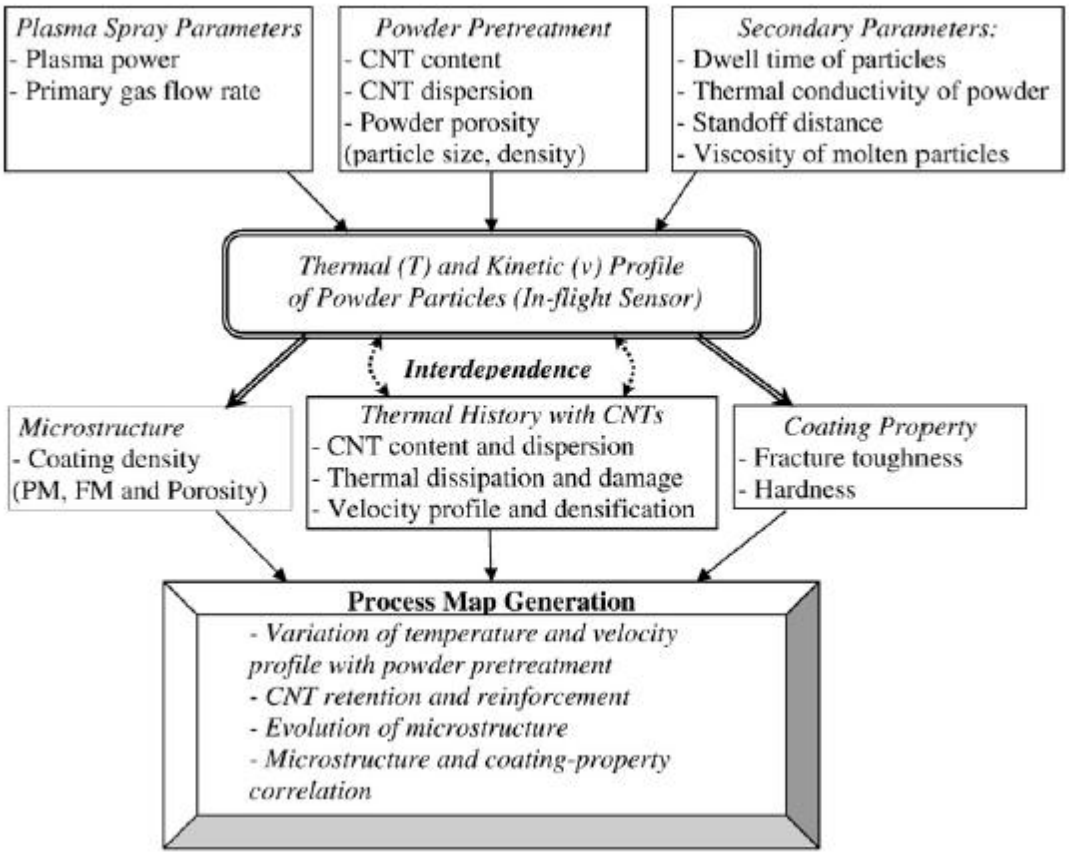

Figure 33: Schematic eliciting effect of thermal and kinetic profile of powder particles in resulting consequent microstructure and material properties. Reprinted with permission from [107].

Correspondingly, it was observed that presence of 4 wt.% CNTs in agglomerated form in A4C-B coating (also limited to CNT distribution on surface of powder agglomerate) lead to accumulation of heat and enhanced the temperature of the powder agglomerate as it passes through plasma plume. Contrastingly, the dispersion of 4 wt.% CNTs in Al_2O_3 matrix (A4C-SD) decreased the thermal damage to the powders in the plasma plume. A further decrease in the thermal exposure was achieved when the content of dispersed CNTs was increased to 8 wt.% in Al_2O_3 matrix. This observation indicated that CNTs trap the heat when present on the surface and the thermal conductivity of the remaining mass and presence of CNTs inside the powder agglomerate reduces the surface damage by absorbing the thermal radiation. A process map eliciting the dwell time of powder agglomerates and consequent development of thermal history is presented in Fig. 34.

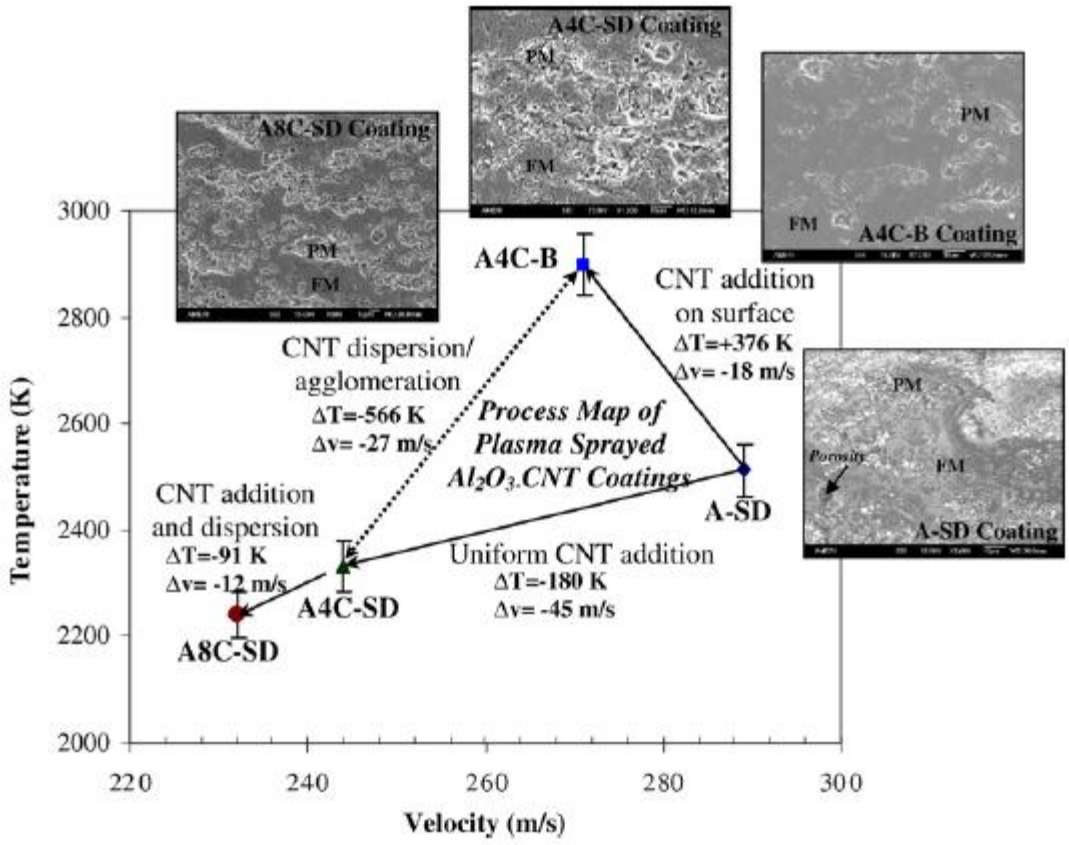

Figure 34: Process map eliciting the thermal and kinetic profiles of A-SD, A4C-B, A4C-SD and A8C-SD plasma sprayed coatings. Reprinted with permission from [107].

Additionally, it was attempted to understand the role of dispersed CNTs in impeding the grain boundary mobility with varying thermal history. It is interesting to correlate whether the temperature or the dwell time plays a dominating role in directing the grain growth, and affecting the grain boundary mobility. Additionally, CNT content might also be responsible for serving as pinning centers towards impediment of the grain growth. Thereby, plasma sprayed samples and Hot isostatically pressed (HIPed) samples were processed towards eliciting the role of grain size, thermal history and kinetic profile in dictating grain boundary mobility. The overall microstructure showing grain sizes 0.52 – 0.79 μm, 0.18-0.32 μm, and 0.15-0.25 μm for the plasma sprayed A-SD, A4C-SD, and A8C-SD respectively is presented in Fig. 35. Reduction in the grain size, when the starting particle size was 0.15 μm clearly confirms the impediment of grain growth with the increasing content of dispersed CNTs.

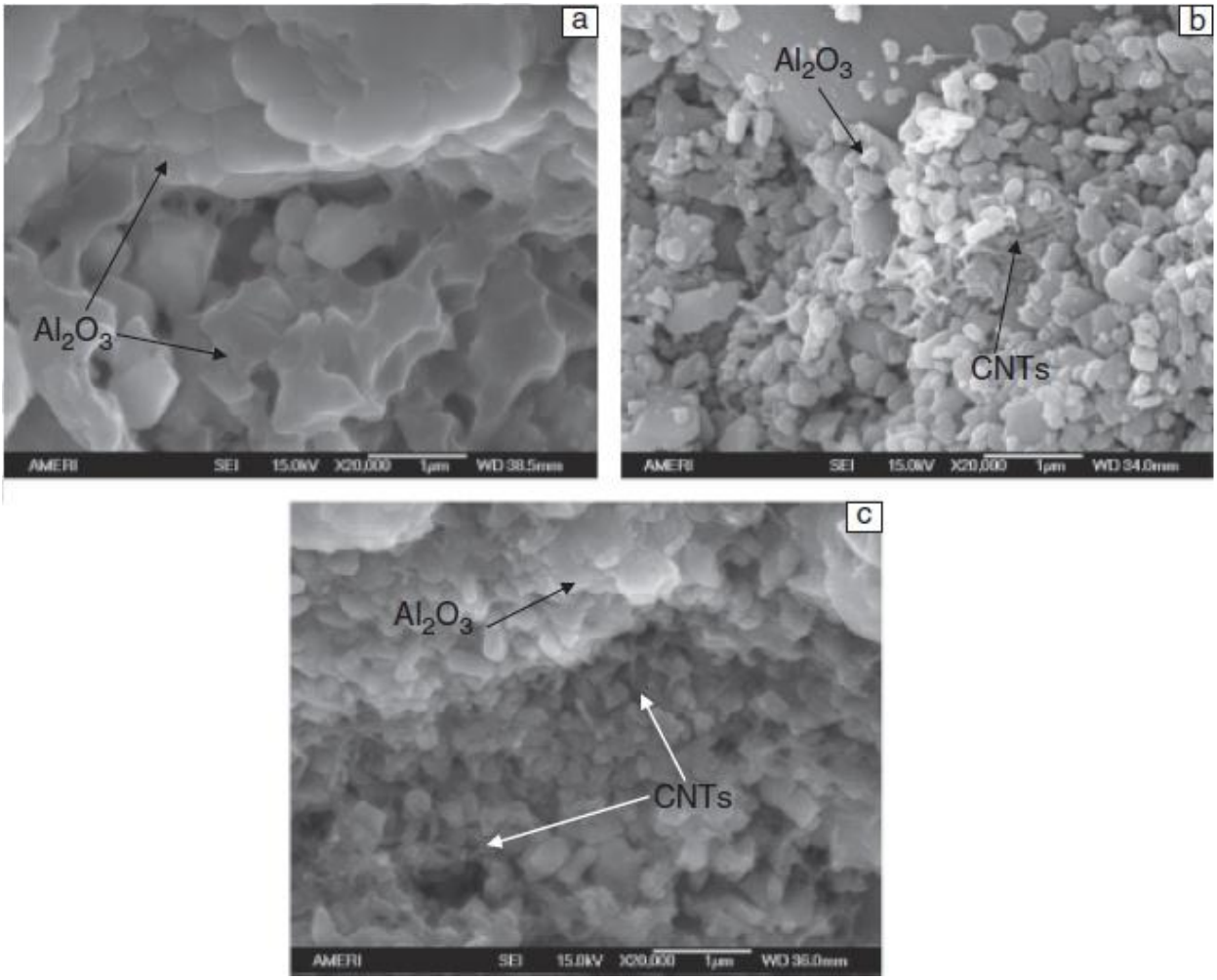

Figure 35: SEM micrographs showing grain size of plasma sprayed (a) A-SD, (b) A4C-SD and (c) A8C-SD coatings. Reprinted with permission from [90].

It can be observed from table 4 that grain boundary mobility are in the range of 1.2 – 4.7 ($\times 10^{-10}$ m^3/N/s, which are around two orders of magnitude greater than that reported in the literature. Higher mobilities in these composites were attributed to the very fine particle size (~150 nm) of the starting feedstock. Additionally, the errors in estimating the grain boundary mobility can extend upto one order of magnitude owing to the thermal gradients inherent in the plasma spray processing. But, definitely, a decrease in the grain boundary constant by four orders of magnitude and reduction of grain boundary mobility by up to four times with increasing CNT content is observed, Table 4.

Table 4: Factors affecting grain growth kinetics for CNT - alumina during plasma spraying. Reprinted with permission from [90].

Coating	Initial Grain Size (G_a, μm)	Final Grain Size (G_n, μm)	WI* porosity (%)	Inflight particle (Temperature,K)	Dwell time ($\times 10^{-4}$ s)	$\frac{1}{G_n} - \frac{1}{G_a}$ ($\times 10^6$ m^{-1})	Grain growth constant ($\times 10^{-3}$K m^2/s)	Grain mobility ($\times 10^{-10}$ m^3/N/s)
A-SD	0.15	0.52-0.79	13.0	2512	3.46	4.7-5.4	3.32-9.89	4.7±1.4
A4C-SD	0.15	0.18-0.32	9.8	2332	4.10	1.2-3.5	0.19-0.39	1.5±0.6
A8C-SD	0.15	0.15-0.25	6.0	2241	4.31	0.13-2.7	0.0003-0.0374	1.2±0.4

WI*=water immersion; CNT=carbon nanotube; SD=spray dried

Presence of undamaged CNT serves as an obstacle to grain growth by pinning the grain boundary motion, Fig. 36. Further, a thinner grain boundary layer (~2 nm) is generated in the A4C-SD sample between A_2O_3 and CNT, whereas this layer extends to ~ 5 nm in A8C-SD plasma

sprayed sample, Fig. 37. Presence of CNTs at the grain boundary regions also indicate that a pinning effect is more effective as CNTs also have shown to form an interface with Al_2O_3 matrix, Fig. 37.

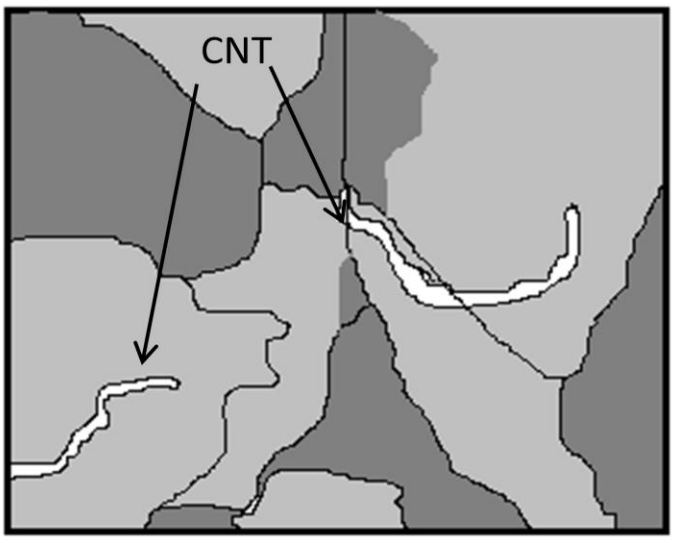

Fig. 36: CNT reinforcement serving as obstacle for grain growth. Adapted from [90].

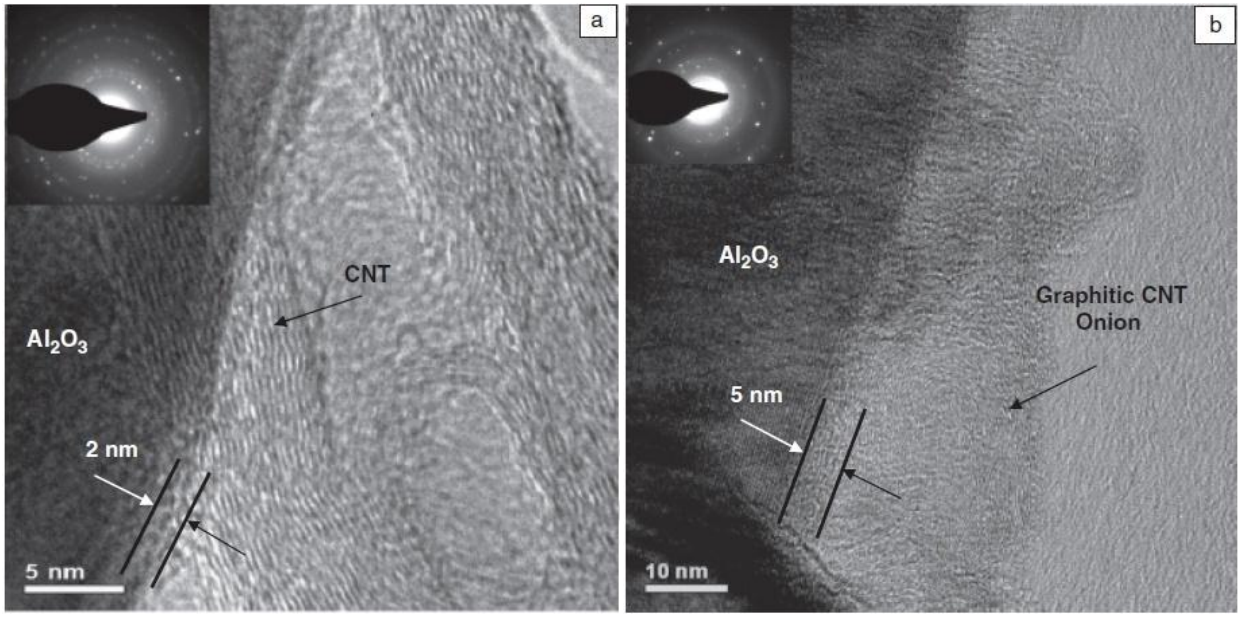

Figure 37: Interfacial layer thickness due to increase in CNT content. (a) A4C-SD (b)A8C-SD. Reprinted with permission from [90].

Following the plasma spraying, hot isostatic pressing (HIPing) was performed on the samples at 1773 K to convert the γ phase into α phase of alumina. Fractured surface of HIPed samples is shown via SEM in Fig. 38, where grain growth is observed, i.e. A-SD, A4C-SD and A8C-Sd showing grain sizes of 1.66-3.46 µm, 1.48-3.47 µm, and 1.04-2.70 µm respectively. Hence, it is clearly indicated that despite lower initial grain sizes of the plasma sprayed samples, CNTs do render grain pinning effect via restricting grain boundary mobility.

Densification has occurred after HIPing and porosity of all the samples has decreased to less than 6 %, Table 5. CNT induce densification by occupying the porous sites, which otherwise get retained as closed porosity [89]. To comment on the effect of temperature and dwell time, Table 5, elicits the grain boundary mobility of HIPed samples in the range of 2-24 x 10^{-17} m^3/N/s, which comes out to be six to seven orders of magnitude lower than that of plasma sprayed coatings, Table 4. It clearly implies that longer durations of holding (1.13 x 10^{-4} s) at lower temperatures (1773 K)

resulted lower grain mobilities (six to seven orders of magnitude) when compared to that of shorter duration of dwell time (3.5-4.5 x 10^{-4} s) at higher temperatures (2241-2512 K).

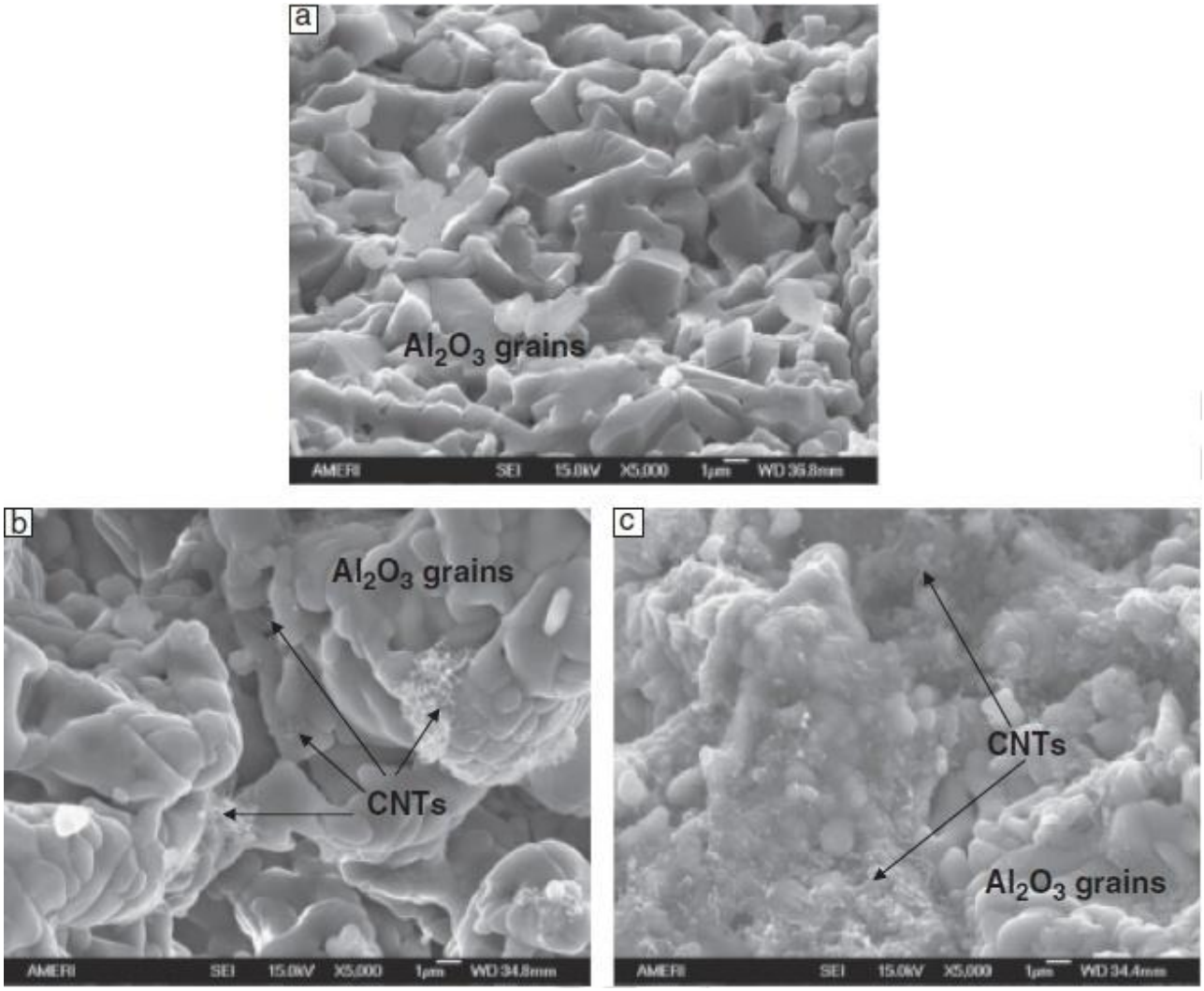

Figure 38: SEM images of SD hot isostatic pressed (HIP) coatings illustrating rise in grain size and the nature of distribution of CNT. (a)A-SD (b)A4C-SD (c)A8C-SD. Reprinted with permission from [90].

Table 5: Factors affecting grain growth kinetics for plasma sprayed alumina-CNT during hot isostatic pressing. Reprinted with permission from [90].

Coating	Initial Grain Size (G_a, μm)	Temp. (K)	Final Grain Size (G_n, μm)	WI* porosity (%)	Dwell time ($\times 10^4$ s)	$\frac{1}{G_n} - \frac{1}{G_a}$ ($\times 10^6$ m^{-1})	Grain boundary mobility ($\times 10^{-17} m^3/N/s$)
A-SD	0.52-0.79	1773	1.66-3.46	5.9	1.13	0.66-1.63	17.5-24.1
A4C-SD	0.18-0.32	1773	1.48-3.47	4.4	1.13	2.84-4.77	3.63-12.7
A8C-SD	0.15-0.25	1773	1.04-2.70	4.0	1.13	5.49-6.08	2.15-5.59

WI*=water immersion; CNT=carbon nanotube; SD=spray dried.

Consequently, the CNT reinforcement remain effective even at plasma spraying temperatures as the lowering of grain boundary mobility is observed, Fig. 39. Additionally, coarser grain size available for grain growth (from plasma sprayed samples to their HIPing) rendered reduced grain mobility, in comparison to the finer grain sizes available during plasma spraying. Hence bigger grains show hindered grain mobility. Moreover, negative slopes in Fig. 39 indicates impediment of grain boundary mobility with increasing CNT content, but the slope being more

negative in HIPed samples indicate the role of reinforcement (CNT) content is stronger when the temperatures are lower.

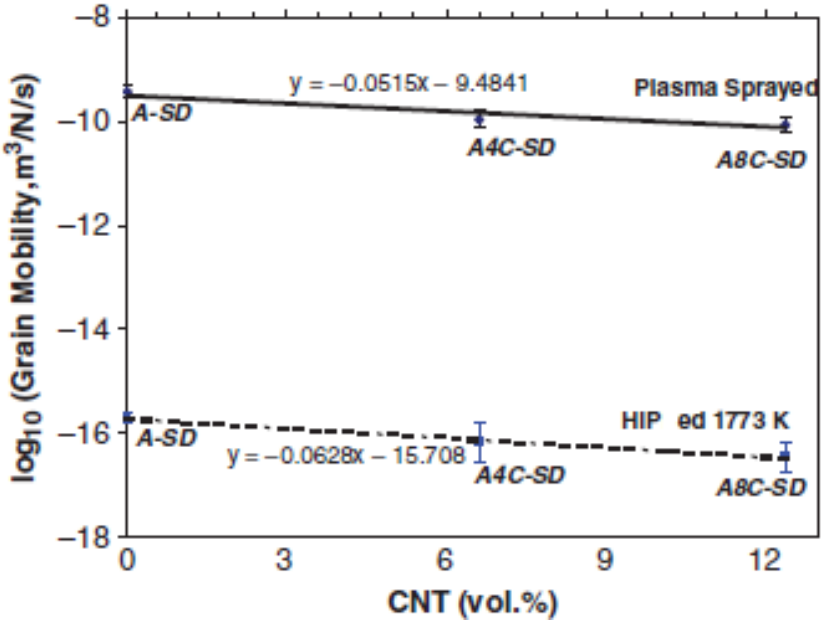

Figure 39: Grain boundary mobility of HIPed and Plasma Sprayed Coatings. Reprinted with permission from [90].

Role of undamaged CNTs present uniformly throughout the matrix act as a sink towards protecting the matrix and reducing thermal exposure. In addition an increase in the grain boundary interface area accommodates grain boundary transition among adjacent grain orientation. Thus, grains are stabilized eliciting reduced grain boundary mobility and tendency for grain growth reduces.

Conclusions

In conclusion, annihilation of grain boundaries depends on the stability it can attain from the angle it makes with the adjacent grains, and number of grains that surrounds. Since, nanocrystalline grain boundaries provide impediment to the dislocation, the inverse Hall Petch relation dominates at grain sizes lower than ~ 25 nm. Hence a control is required on the grain engineering to achieve superior mechanical properties while tailoring the transport across grain boundaries. Grain boundary kinetics strongly depends on the dopants present in alumina, defining various transitions or complexions that dictate the grain boundary mobility while rendering solute drag effects. Overall, six complexions starting from a clean boundary to various boundary layer thickness and to a rough grain boundary interface were defined. Various dopants (such as calcia and magnesia) have shown to enhance and reduce the grain boundary mobility since the complexions predominant at the grain boundary interface are highly different. Pre-wetting, wetting and clean boundary regimes are also observed and they are stable at higher temperatures. Role of carbon nanotubes (CNTs) in impeding the grain boundary mobility is elicited with a difference in the grain boundary layer thickness. It was also concluded that lower grain size and acute thermal exposure renders a stronger role in enhancing grain boundary mobility in comparison to that of coarser grain size, and prolonged time.

Acknowledgement:

Authors acknowledge research grant support from the Department of Biotechnology, India.

References:

[1] I. Levin, D. Brandon: J. Am. Ceram. Soc. Vol. 81 (1998), p. 1995.

[2] M. U. Devi: Ceramics International Vol. 30 (2004), p. 555.

[3] R. M. Pherson: Journal of Materials Science Vol. 8 (1973), p. 851.

[4] H. Knozinger, P. Ratnasamy: Catalysis Reviews- Science and Engineering Vol. 17 (1985), p. 31.

[5] G. Poncelet, P. A. Jacobs, P. Grange, B. Delmon: Elsevien, Amsterdam Vol. (1991), p. 95.

[6] G. Paglia, Ph.D. thesis, Curtin University of Technology, 2004.

[7] B. Lux, C. Colombier, H. Altena, K. Stjernberg: Thin Solid Films Vol. 138 (1986), p. 49.

[8] C. Ruberto, Y. Yourdshahyan, B.I. Lundqvist: Physical Review B Vol. 67 (2003), p. 195412.

[9] S. Vuorinen, J. Skogsmo: Thin Solid Films Vol. 193 (1990), p. 536.

[10] K. Nishio, M. Neo, H. Akiyama: Journal of Biomedical Materials Research Vol. 55 (2001), p. 164.

[11] W. C. Wei, S. J. Lu, C. L. Hsieh: Journal of the Ceramic Society of Japan Vol. 104 (1996), p. 277.

[12] H.C. Kao, W. C. Wei: J. Am. Ceram. Soc. Vol. 83 (2000), p. 362.

[13] L. Jon Martin Andersson: Science and Technology, Dissertation No. 987 Vol. p.

[14] E. Wallin, J.M. Andersson, V. Chirit, U. Helmersson: J. Phys.: Condens. Matter Vol. 16 (2004), p. 8971.

[15] D. Fargeot, D. Mercurio, A. Dauger: Materials Chemistry and Physics Vol. 24 (1990), p. 299.

[16] I. Levin, D. Brandon: J. Am. Ceram. Soc. Vol. 81 (1998), p. 1995.

[17] J. Felsche: Zeitschrift. fUr Kl'istallographie, Bd. Vol. 127 (1968), p. 94.

[18] J. M. Newsam: Solid State Ionics Vol. 6 (1982), p. 129.

[19] Z. Skotniczny, J. Moscinski, Z. Rycerz: J. Phys. C: Solid State Phys Vol. 19 (1986), p. 4781.

[20] H. C. Stumpf, A. S. Russell, J. W. Newsome, C. M. Tucker: Ind. Eng. Chem. Vol. 42 (1950), p. 1398.

[21] H. Saalfeld, in: “Structure Phases of Dehydrated Gibbsite” in p. 310–15 in Reactivity of Solid, edited by J. H. de Boer Elsevier, Amsterdam, The Netherlands(1961).

[22] I. Levin, D. G. Brandon: Philosophical Magazine Letters Vol. 77 (1998), p. 117.

[23] S. D. Kenny, D. Nguyen-Manh, H. Fujitani, A. P. Sutton: Philosophical Magazine Letters Vol. 78 (1998), p. 469.

[24] H. V. Atkinson: Acta metall Vol. 36 (1988), p. 469.

[25] V. Raghvan, in: *Solid State Phase Transformation* /Prentice Hall of India Pvt. Ltd. New Delhi (1992).

[26] Burger, in: *Elementry Crystallography; An introduction to the fundamental geometrical features of crystals* / John Wiley & Sons Inc. New York (1963).

[27] B. D. Cullity, in: *Elements of X-ray Diffraction* /Addison-Wesley Publishing Company, Inc. Reading, Massachusetts (1956).

[28] J. W.D. Callister, in: *Materials Science & Engineering An Introduction* /John Wiley & Sons, Inc. Singapore (2001).

[29] G. E. Dieter, in: *Mechanical Metallurgy* /McGraw-Hill Book Company London (1988).

[30] Information on www.nanowrek.com/nanotechnology/introduction

[31] M. A. Meyers, A. Mishra, D. J. Benson: Progress in Materials Science Vol. 51 (2006), p. 427.

[32] P. G. Sanders, J.A.Eastman, J.R.Weertman: Acta Mater Vol. 45 (1997), p. 4019.

[33] J. K. Mackenzie: Proc. Phys. Soc. B Vol. 63 (1950), p. 2.

[34] J. B. Wachtman, in: *Mechanical and thermal properties of ceramics* NBS Washington: NBS Special Publication Washington (1963).

[35] F. Fellah, G. Dirras, J. Gubicza, F. Schoenstein, N. Jouini, S. M. Cherif, C. Gatel, J. Douin: Journal of Alloys and Compounds Vol. 489 (2010), p. 424–428.

[36] A. H. Chokshi, A. Rosen, J. Karch, H. Gleiter: Scripta Mater Vol. 23 (1989), p. 1679.

[37] P. P. Chattopadhyay, S. K. Pabi, I. Manna: Z Metallkunde Vol. 91 (2000), p. 1049.

[38] A. A. Fedorov, M. Y. Gutkin, I. A. Ovid'ko: Scripta Materialia Vol. 47 (2002), p. 51.

[39] H. Conrad, J. Narayan: Scripta Materialia Vol. 42 (2000), p. 1025.

[40] H. S. Cao: Materials Latters Vol. 58 (2004), p. 3564.

[41] Y. F. Shen, X. H. Chen, B. Wu, L. Lu, "Microstructure and Tensile Strength of Cu with Nano-Scale Twins", presented at *IUTAM Symposium on Mechanical Behavior and Micro-Mechanics of Nanostructured Materials*/ Springer, Netherlands (2007).

[42] H. Tanimoto, S. Sakai, H. Mizubayashi: Nano Stuructured Materials Vol. 12 (1999), p. 751.

[43] C. C. Koch: Journal of Metastable and Nanocrystalline Vol. 18 (2003), p. 9.

[44] C. Zheng, Y.W. Zhang: Journal of Nanomaterials Vol. (2007), p. 6.

[45] D. T. Jiang, D. M. Hulbert, U. A. Tamburini, T. Ng, D. Land, A.K. Mukherjee: J. Am. Ceram. Soc. Vol. 91 (2008), p. 151.

[46] M. Stuer, Z. Zhao, U. Aschauer, P. Bowen, Journal of the European Ceramic Society Vol. 30 (2010), p. 1335.

[47] J. K. A.Krell, T. Hutzler: Journal of the European Ceramic Society Vol. 29 (2009), p. 275.

[48] M. Lebedev, S. Krumdieck: Current Applied Physics Vol. 8 (2008), p. 233.

[49] O. Zywitzki, G. Hoetzsch: Surf. Coat. Technol. Vol. 88 (1996), p. 640.

[50] T. Hubert, S. Svoboda, B. Oertel: Surf. Coat. Technol. Vol. 201 (2006), p. 487.

[51] J. Wang, S. Yang, M. Chen, Q. Xue: Surf. Coat. Technol. Vol. 176 (2004), p. 229.

[52] C. B. Cao, Q. Fu, H. S. Zhu: Thin Solid Films Vol. 348 (1999), p. 99.

[53] B. Hirschauer, S. Soderholm, G. Chiaia, U. O. Karlsson: Thin Solid Films Vol. 305 (1997), p. 243.

[54] N. Bahalawane: Surf. Coat. Technol. Vol. 200 (2006), p. 4097.

[55] J. Akedo, M. Lebedev: Jpn. J. Appl. Phys. Vol. 38 (1999), p. 5397.

[56] M. Lebedev, J. Akedo, T. Ito: J. Cryst. Growth Vol. 275 (2005), p. e1301.

[57] H. K. Pulker: Appl. Opt. Vol. 18 (1979), p. 1969.

[58] A. Braun, G. Falk, R. Clasen: Materialwiss. Werkstofftech Vol. 37 (2006), p. 293.

[59] D. Goslinski, M. Kuntz, G. Grathwohl: J. Am. Ceram. Soc. Vol. 85 (2002), p. 2449.

[60] A. C. F. Cocks, S. P. A. Gill: Acta Materialia Vol. 44 (1996), p. 4765.

[61] T. O. Saetre: Modeling and Simulation in Materials Science and Engineering Vol. 12 (2004), p. 1267.

[62] H. C. H. Carpenter, C. F. Elam: J. Inst. Met. Vol. 24 (1920), p. 83.

[63] T. Sutoki: Sci. Rep. Tohuku Univ. Vol. 178 (1928), p. 857.

[64] D. Harker, E. R. Parker: Trans. Am. Soc. Met. Vol. 34 (1945), p. 156.

[65] J. Czochralski: Int. Z. Metallogr. Vol. 6 (1914), p. 289.

[66] J. A. Ewing, W. Rosenhain: Phil. Trans. R. Soc. Lond. A Vol. 193 (1900), p. 353.

[67] J. E. Burke, D. Turnbull: Prog. Metal Phys. Vol. 3 (1952), p. 220.

[68] C. S. Smith: Metal Interf. Vol. 3 (1952), p. 65.

[69] M.A. Fortes, A.C. Ferro: Acta Metall. Vol. 33 (1985), p. 1697.

[70] W. W. Mullins: Journal of Applied Physics Vol. 27 (1956), p. 900.

[71] J. V. Neumann: Metal Interfaces, ASM, Cleveland, Ohio, USA Vol. (1952), p. 108.

[72] V. E. Fradkov, M. E. Glicksman, M. Palmer, J. Nordberg, K. Rajan: Physica D Vol. 66 (1993), p. 50.

[73] M. A. Palmer, M. E. Glicksman, K. Rajan: Scripta Materialia Vol. 48 (2003), p. 1173.

[74] D. Weaire, N. Rivier: Contemporary Physics Vol. 25 (1984), p. 59.

[75] P. Blikstein, A. P. Tschiptschin: Materials Research Vol. 2 (1999), p. 133.

[76] J. Fletcher, "Three-Dimensional Grain Growth Model Using the Phase Field Approach" Information on www.csm.ornl.gov/lnternships/rams _ 05/abstracts/Lfletcher. pdf

[77] H. J. Frost , C. V. Thompson: Solid State & Materials Science Vol. 1 (1996), p. 361.

[78] V. Tikare, E. A. Holm, D. Fan **,** L. Q. Chen: Acta Mate Vol. 47(1999), p. 6208.

[79] P. R. Rios, G. Gottstein, L. S. Shvindlerman: Materials Science and Engineering A Vol. 332 (2002), p. 231.

[80] F. J. G. J. M. Guilemany: Intermetallics Vol. 6 (1998), p. 445.

[81] H. T. G. Hentzell, B. Andersson, S. E. Karlsson: Acta metall Vol. 31 (1983), p. 2103.

[82] Z. Chen,Z. He, W. Jie: Transactions of Nonferrous Metals Society of China Vol. 19 (2009), p. 410.

[83] T. Takasugi, O. Izumi: Acta metall Vol. 33 (1985), p. 49.

[84] E. Manor: NanoStructured Materials Vol. 8 (1997), p. 359.

[85] A. B. Cota, C. A. M. Lacerda, F. L. G. Oliveira, F. A. Machado, F. G. de S. Araújo: Scripta Materialia Vol. 51 (2004), p. 721.

[86] Y.H. Lee, S. Y. Lee, I. H. Son, Y. S. Park, D.L. Lee: POSCO TECHNICAL REPORT Vol. 10 (2007), p. 79.

[87] S. J. Dillon, M. Tang, W. C. Carter, M. P. Harmer: Acta Materialia Vol. 55 (2007), p. 6208.

[88] J. W. Cahn: Acta Metallurgica Vol. 10 (1962), p. 789.

[89] S. J. Dillon, S. K. Behera, M. P. Harmer: Acta Materialia Vol. 56 (2008), p. 1374.

[90] K. Balani, S. R. Bakshi, D. Lahiri, A. Agarwal: Int. J. Appl. Ceram. Technol. Vol. (2009), p. DOI:10.1111/j.1744.

[91] A. Subramaniam, C. T. Koch, R. M. Cannon, M. Ruhle: Materials Science and Engineering A Vol. 422 (2006), p. 3.

[92] J. W. Cahn: J. Chem. Phys. Vol. 66 (1977), p. 3667.

[93] S. J. Dillon, M. P. Harmer: Acta materialia Vol. 55 (2007), p. 5247.

[94] R. M. Cannon, M. Rühle, M. J. Hoffmann, R. H. French, H. Gu, A. P. Tomsia, E. Saiz: J. Am. Ceram. Soc. Vol. 118 (2000), p. 427.

[95] S. J. Dillon, M. P. Harmer: J. Am. Ceram. Soc. Vol. 90 (2007), p. 993.

[96] C. Scott, M. Kaliszewski, C. Greskovich, L. Levinson: J. Am. Ceram. Soc. Vol. 85 (2002), p. 1275.

[97] J. Cho, H. P. Harmer, H. M. Chan, J. M. Rickman, A. M. Thompson: J. Am. Ceram. Soc. Vol. 80 (1997), p. 1013.

[98] O. A. Ruano, J. Wadsworth, O. D. Sherby: Acta Mater Vol. 51 (2003), p. 3617.

[99] P. Hou: J. Am. Ceram. Soc. Vol. 86 (2003), p. 660.

[100] Y. M. Kim, S. H. Hong, D. Y. Kim: J. Am. Ceram. Soc. Vol. 83 (2000), p. Kim Y.

[101] I. MacLaren, R. M. Cannon, M. A. Gu¨lgu¨n, R. Voytovych, N. P.-. Pogrion, C. Scheu: J. Am. Ceram. Soc. Vol. 86 (2003), p.:650.

[102] D. R. Clarke: J. Am. Ceram. Soc. Vol. 70 (1987), p. 15.

[103] S. I. Bae, S. Baik: J .Am. Ceram. Soc. Vol. 76 (1993), p. 1065.

[104] S. J. Dillon, M. P. Harmer: J. Am. Ceram. Soc. Vol. 90 (2007), p. 996.

[105] C. M. Wang, H. M. Chan, M. P. Harmer: J. Am. Ceram. Soc. Vol. 87 (2004), p. 378.

[106] I. MacLaren, R. M. Canon, M. A. Gulgun, R. Voytovych, N. P. Pogrion, C. Scheu, U. Taffner, M. Ruhle: J. Am. Ceram. Soc. Vol. 86 (2003), p. 650.

[107] K. Balani, A. Agarwal: Surf. Coat. Tech. Vol. 202 (2008), p. 4270.

Thermal and Thermodynamic Stability of Nanomaterials
10.4028/www.scientific.net/MSF.653

Grain Growth Behavior of Al_2O_3 Nanomaterials: A Review
10.4028/www.scientific.net/MSF.653.87

DOI References
[5] G. Poncelet, P. A. Jacobs, P. Grange, B. Delmon: Elsevien, Amsterdam Vol. (1991), p. 95.
10.1016/S0167-2991(08)64565-6
[7] B. Lux, C. Colombier, H. Altena, K. Stjernberg: Thin Solid Films Vol. 138 (1986), p. 49.
10.1016/0040-6090(86)90214-2
[8] C. Ruberto, Y. Yourdshahyan, B.I. Lundqvist: Physical Review B Vol. 67 (2003), p. 95412.
10.1103/PhysRevB.67.195412
[9] S. Vuorinen, J. Skogsmo: Thin Solid Films Vol. 193 (1990), p. 536.
10.1016/S0040-6090(05)80063-X
[10] K. Nishio, M. Neo, H. Akiyama: Journal of Biomedical Materials Research Vol. 55 (2001), . 164.
10.1002/1097-4636(200105)55:2<164::AID-JBM1003>3.3.CO;2-T
[14] E. Wallin, J.M. Andersson, V. Chirit, U. Helmersson: J. Phys.: Condens. Matter Vol. 16 2004), p. 8971.
10.1088/0953-8984/16/49/012
[15] D. Fargeot, D. Mercurio, A. Dauger: Materials Chemistry and Physics Vol. 24 (1990), p. 99.
10.1016/0254-0584(90)90093-P
[17] J. Felsche: Zeitschrift. fUr Kl'istallographie, Bd. Vol. 127 (1968), p. 94.
10.1524/zkri.1968.127.1-4.94
[18] J. M. Newsam: Solid State Ionics Vol. 6 (1982), p. 129.
10.1016/0167-2738(82)90077-7
[19] Z. Skotniczny, J. Moscinski, Z. Rycerz: J. Phys. C: Solid State Phys Vol. 19 (1986), p. 781.
10.1088/0022-3719/19/24/021
[20] H. C. Stumpf, A. S. Russell, J. W. Newsome, C. M. Tucker: Ind. Eng. Chem. Vol. 42 1950), p. 1398.
10.1021/ie50487a039
[22] I. Levin, D. G. Brandon: Philosophical Magazine Letters Vol. 77 (1998), p. 117.
10.1080/095008398178697
[23] S. D. Kenny, D. Nguyen-Manh, H. Fujitani, A. P. Sutton: Philosophical Magazine Letters Vol. 78 (1998), p. 469.
10.1080/095008398177698
[31] M. A. Meyers, A. Mishra, D. J. Benson: Progress in Materials Science Vol. 51 (2006), p. 27.
10.1016/j.pmatsci.2005.08.003
[32] P. G. Sanders, J.A.Eastman, J.R.Weertman: Acta Mater Vol. 45 (1997), p. 4019.
10.1016/S1359-6454(97)00092-X
[35] F. Fellah, G. Dirras, J. Gubicza, F. Schoenstein, N. Jouini, S. M. Cherif, C. Gatel, J. Douin: ournal of Alloys and Compounds Vol. 489 (2010), p. 424–428.
10.1016/j.jallcom.2009.09.153
[36] A. H. Chokshi, A. Rosen, J. Karch, H. Gleiter: Scripta Mater Vol. 23 (1989), p. 1679.
10.1016/0036-9748(89)90342-6
[38] A. A. Fedorov, M. Y. Gutkin, I. A. Ovidko: Scripta Materialia Vol. 47 (2002), p. 51.
10.1016/S1359-6462(02)00096-9

[39] H. Conrad, J. Narayan: Scripta Materialia Vol. 42 (2000), p. 1025.
10.1016/S1359-6462(00)00320-1
[43] C. C. Koch: Journal of Metastable and Nanocrystalline Vol. 18 (2003), p. 9.
10.4028/www.scientific.net/JMNM.18.9
[44] C. Zheng, Y.W. Zhang: Journal of Nanomaterials Vol. (2007), p. 6.
10.1155/2007/64589
[45] D. T. Jiang, D. M. Hulbert, U. A. Tamburini, T. Ng, D. Land, A.K. Mukherjee: J. Am. eram. Soc. Vol. 91 (2008), p. 151.
10.1111/j.1551-2916.2007.02086.x
[46] M. Stuer, Z. Zhao, U. Aschauer, P. Bowen, Journal of the European Ceramic Society Vol. 0 (2010), p. 1335.
10.1016/j.jeurceramsoc.2009.12.001
[48] M. Lebedev, S. Krumdieck: Current Applied Physics Vol. 8 (2008), p. 233.
10.1016/j.cap.2007.10.057
[49] O. Zywitzki, G. Hoetzsch: Surf. Coat. Technol. Vol. 88 (1996), p. 640.
10.1016/0257-8972(95)00270-7
[50] T. Hubert, S. Svoboda, B. Oertel: Surf. Coat. Technol. Vol. 201 (2006), p. 487.
10.1016/j.surfcoat.2005.11.014
[52] C. B. Cao, Q. Fu, H. S. Zhu: Thin Solid Films Vol. 348 (1999), p. 99.
10.1016/S0040-6090(99)00023-1
[53] B. Hirschauer, S. Soderholm, G. Chiaia, U. O. Karlsson: Thin Solid Films Vol. 305 (1997), . 243.
10.1016/S0040-6090(97)00151-X
[56] M. Lebedev, J. Akedo, T. Ito: J. Cryst. Growth Vol. 275 (2005), p. e1301.
10.1016/j.jcrysgro.2004.11.109
[57] H. K. Pulker: Appl. Opt. Vol. 18 (1979), p. 1969.
10.1364/AO.18.001969
[58] A. Braun, G. Falk, R. Clasen: Materialwiss. Werkstofftech Vol. 37 (2006), p. 293.
10.1002/mawe.200600003
[59] D. Goslinski, M. Kuntz, G. Grathwohl: J. Am. Ceram. Soc. Vol. 85 (2002), p. 2449.
10.1021/jm020827z
[60] A. C. F. Cocks, S. P. A. Gill: Acta Materialia Vol. 44 (1996), p. 4765.
10.1016/S1359-6454(96)00121-8
[65] J. Czochralski: Int. Z. Metallogr. Vol. 6 (1914), p. 289.
10.1007/BF01546358
[66] J. E. Burke, D. Turnbull: Prog. Metal Phys. Vol. 3 (1952), p. 220.
10.1016/0502-8205(52)90009-9
[69] M.A. Fortes, A.C. Ferro: Acta Metall. Vol. 33 (1985), p. 1697.
10.1016/0001-6160(85)90164-6
[70] W. W. Mullins: Journal of Applied Physics Vol. 27 (1956), p. 900.
10.1063/1.1722511
[71] V. E. Fradkov, M. E. Glicksman, M. Palmer, J. Nordberg, K. Rajan: Physica D Vol. 66 (1993), p. 50.
10.1016/0167-2789(93)90223-N
[72] V. E. Fradkov, M. E. Glicksman, M. Palmer, J. Nordberg, K. Rajan: Physica D Vol. 66 1993), p. 50.
10.1016/0167-2789(93)90223-N
[73] M. A. Palmer, M. E. Glicksman, K. Rajan: Scripta Materialia Vol. 48 (2003), p. 1173.
10.1016/S1359-6462(02)00582-1

[74] D. Weaire, N. Rivier: Contemporary Physics Vol. 25 (1984), p. 59.
10.1080/00107518408210979
[75] P. Blikstein, A. P. Tschiptschin: Materials Research Vol. 2 (1999), p. 133.
10.1590/S1516-14391999000300004
[78] P. R. Rios, G. Gottstein, L. S. Shvindlerman: Materials Science and Engineering A Vol. 332 (2002), p. 231.
10.1016/S0921-5093(01)01745-2
[79] P. R. Rios, G. Gottstein, L. S. Shvindlerman: Materials Science and Engineering A Vol. 332 2002), p. 231.
10.1016/S0921-5093(01)01745-2
[80] F. J. G. J. M. Guilemany: Intermetallics Vol. 6 (1998), p. 445.
10.1016/S0966-9795(97)00041-1
[81] H. T. G. Hentzell, B. Andersson, S. E. Karlsson: Acta metall Vol. 31 (1983), p. 2103.
10.1016/0001-6160(83)90029-9
[83] T. Takasugi, O. Izumi: Acta metall Vol. 33 (1985), p. 49.
10.1016/0001-6160(85)90218-4
[84] E. Manor: NanoStructured Materials Vol. 8 (1997), p. 359.
10.1016/S0965-9773(97)00176-1
[87] S. J. Dillon, M. Tang, W. C. Carter, M. P. Harmer: Acta Materialia Vol. 55 (2007), p. 6208.
10.1016/j.actamat.2007.07.029
[88] J. W. Cahn: Acta Metallurgica Vol. 10 (1962), p. 789.
10.1016/0001-6160(62)90092-5
[89] S. J. Dillon, S. K. Behera, M. P. Harmer: Acta Materialia Vol. 56 (2008), p. 1374.
10.1016/j.actamat.2007.11.042
[90] A. Subramaniam, C. T. Koch, R. M. Cannon, M. Ruhle: Materials Science and Engineering A Vol. 422 (2006), p. 3.
10.1016/j.msea.2006.01.004
[91] A. Subramaniam, C. T. Koch, R. M. Cannon, M. Ruhle: Materials Science and Engineering Vol. 422 (2006), p. 3.
10.1016/j.msea.2006.01.004
[92] J. W. Cahn: J. Chem. Phys. Vol. 66 (1977), p. 3667.
10.1063/1.434402
[93] S. J. Dillon, M. P. Harmer: Acta materialia Vol. 55 (2007), p. 5247.
10.1016/j.actamat.2007.04.051
[95] S. J. Dillon, M. P. Harmer: J. Am. Ceram. Soc. Vol. 90 (2007), p. 993.
10.1111/j.1551-2916.2007.01510.x
[96] C. Scott, M. Kaliszewski, C. Greskovich, L. Levinson: J. Am. Ceram. Soc. Vol. 85 (2002), . 1275.
10.1111/j.1151-2916.2002.tb00257.x
[97] J. Cho, H. P. Harmer, H. M. Chan, J. M. Rickman, A. M. Thompson: J. Am. Ceram. Soc. ol. 80 (1997), p. 1013.
10.1111/j.1151-2916.1997.tb02936.x
[98] O. A. Ruano, J. Wadsworth, O. D. Sherby: Acta Mater Vol. 51 (2003), p. 3617.
10.4028/www.scientific.net/MSF.426-432.11
[99] P. Hou: J. Am. Ceram. Soc. Vol. 86 (2003), p. 660.
10.1111/j.1151-2916.2003.tb03355.x
[103] S. I. Bae, S. Baik: J .Am. Ceram. Soc. Vol. 76 (1993), p. 1065.

10.1111/j.1151-2916.1993.tb05338.x
[104] S. J. Dillon, M. P. Harmer: J. Am. Ceram. Soc. Vol. 90 (2007), p. 996.
10.1111/j.1551-2916.2007.01512.x
[105] C. M. Wang, H. M. Chan, M. P. Harmer: J. Am. Ceram. Soc. Vol. 87 (2004), p. 378.
10.1111/j.1551-2916.2004.00378.x
[106] I. MacLaren, R. M. Canon, M. A. Gulgun, R. Voytovych, N. P. Pogrion, C. Scheu, U. affner, M. Ruhle: J. Am. Ceram. Soc. Vol. 86 (2003), p. 650.
10.1111/j.1151-2916.2003.tb03354.x
[107] K. Balani, A. Agarwal: Surf. Coat. Tech. Vol. 202 (2008), p. 4270.
10.1016/j.surfcoat.2008.03.024